RESONANT FREQUENCY CHARACTERIZATION OF A NOVEL MEMS BASED MEMBRANE ENGINE

By

ROBERT MICHAEL GIFFORD, JR

A thesis submitted in partial fulfillment of
the requirements for the degree of

MASTER OF SCIENCE IN MECHANICAL ENGINEERING

WASHINGTON STATE UNIVERSITY
School of Mechanical and Materials Engineering

August 2004

To the Faculty of Washington State University:

The members of the Committee appointed to examine the thesis of ROBERT MICHAEL GIFFORD, JR find it satisfactory and recommend that it be accepted.

_____
Chair

_____

_____

ACKNOWLEDGEMENT

I have been extremely privileged to work so closely with each of my committee members. I am thankful for the support that each of them has provided. I am especially grateful for the advice and guidance provided by Dr. Cill Richards as my advisor. She has never ceased to make herself available to provide the direction and expertise necessary for me to complete my research. Also, Dr. Bob Richards and Dr. Dave Bahr have been a continuous source of guidance in relation to the engine operation, experimentation, and fabrication.

I would also like to thank the entire P3 engine group, both past and present. Each team member's contributions have been vital to the success of this research. A few people deserve special mention. I am thankful for the patience and knowledge of Scott Whalen and Mike Thompson in teaching me to assemble and operate engines, as well as countless conversations about engine concepts. Kirsten McNeil has been a huge help in experiments, and I wish her the best in continuing studies of engine resonant frequency. Jamie Raupp and Jeong-hyun Cho have been a big help in discussions involving the laser vibrometer.

Dedication

To Amanda Kristyne.

RESONANT FREQUENCY CHARACTERIZATION OF A NOVEL MEMS BASED MEMBRANE ENGINE

Abstract

by Robert Michael Gifford, Jr., M.S.
Washington State University
August 2004

Chair: Cecilia Richards

This thesis provides information regarding the characterization and control of the resonant frequency of the Washington State University P3 Micro Engine. It is essential to establish means to measure and control engine resonant frequency, since resonant operation is vital to the P3 engine operation.

In order to measure the resonant frequency of the engine, a forced-vibration method and a free-vibration method were developed. Using the forced-vibration method, an engine assembled with a 3 mm generator, 75 μm cavity depth, and a 500 mm bubble diameter resulted in a resonant frequency of 10,100 Hz. The same engine was also tested using the free vibration method where a beating frequency was observed in the "after ringing" response. A Fourier transform of the response yielded a resonant mode matching the forced vibration experiment. In order to eliminate the beating frequency an alternate membrane was used. Using the free-vibration method, an engine assembled with a 4 mm silicon membrane, 75 μm cavity depth, and a 1170 um bubble diameter resulted in a resonant frequency of 2037 Hz with an experimental repeatability of +/- 8.6%.

A parametric study was conducted to determine the effects of membrane size, bubble diameter, and cavity thickness on resonant frequency. Results showed that membrane size had a very large effect on resonant frequency. Engines assembled with the same cavity depth but differing silicon membrane side lengths of 3 mm, 4 mm, 6 mm, and 8 mm had average resonant frequencies of 2550 Hz, 1615 Hz, 742 Hz, and 416 Hz, respectively. Bubble diameter had very little effect on resonant frequency, providing only a +/- 8.2% change for bubble diameters ranging from 400 μm to 1500 μm. Three engine cavity depths were tested: 75 μm, 150 μm, and 225 μm for engines assembled with 4 mm silicon membranes and varying bubble diameter. An increase in resonant frequency was seen as the cavity depth was increased. The mean resonant frequencies with 95% confidence for the 75 μm, 150 μm, and 225 μm cavity depths were 1206 ± 206 Hz, 1615 ± 154 Hz, and 2081 ± 291 Hz, respectively. Therefore, membrane size and cavity depth have very good potential to control system resonant frequency.

Finally, a model was developed to serve as a design tool for controlling engine resonant frequency based on system parameters. The model operates under the principles of an added virtual mass factor, relating the resonant frequency of the engine to the theoretical resonant frequency of the upper membrane of the engine in a vacuum. The model was shown to fit the experimental data well. The model was further extrapolated to provide the necessary engine dimensions required to achieve a resonant frequency of 500 Hz.

TABLE OF CONTENTS

Page

ACKNOWLEDGEMENTS……iii

ABSTRACT……v

LIST OF TABLES……...x

LIST OF FIGURES……xi

CHAPTER

1. INTRODUCTION.....1

1.1 Motivation.....1

1.2 Literature Review.....3

1.2.1 Membrane Resonators……..…….…….....3

1.2.2 Membrane Effects……..……..5

1.2.3 Membrane – Fluid Effects…….13

1.2.4 Membrane – Fluid – Cavity Effects…….……..18

1.3 Research Objectives.....20

2. FABRICATION AND EQUIPEMENT.....22

2.1 Engine Fabrication.....22

2.1.1 Membrane Fabrication……..……..…….……..23

2.1.2 Generator Fabrication……24

2.1.3 Heater Fabrication…….26

2.1.4 Engine Assembly……...27

2.2 Equipment…….....30

2.2.1 Pulse System……..……..…….…….30

2.2.2 Laser Interferometer……..…….32

2.2.3 Laser Vibrometer…….……..34

3. MEASURING RESONANT FREQUENCY.....37

3.1 Forced vs. Free Vibration.....37

3.1.1 Forced Vibration Method……..……..…….…….37

3.1.2 Free Vibration Method……..39

3.1.3 Pursuing an Experimental Method……40

3.2 Forced Vibration Experiment.....41

3.3 Free Vibration Experiment…….43

4. ENGINE PARAMETRIC STUDY.....….....53

4.1 Engine Parameters.....53

4.2 Experimental Procedure…….54

4.3 Membrane Geometry…….….56

4.3.1 Membrane Size Experiment……..……..……..…56

4.3.2 Membrane Size Results……..…59

4.4 Bubble Diameter.....60

4.4.1 Bubble Size Experiment……61

4.4.2 Bubble Size Results……...62

4.5 Cavity Depth……...64

4.5.1 Experimental Methods……..…….……64

4.5.2 Cavity Depth Results…….65

5. AVMI FACTOR MODEL.....67

5.1 AVMI Method.....67

5.2 Application to Engine…….69

6. CONCLUSIONS AND RECOMENDATIONS.....79

6.1 Measuring Resonant frequency.....79

6.2 Resonant frequency Parametric Study…….……...80

6.3 AVMI Model……..81

6.4 Recommendations……...82

REFFERENCES……84

LIST OF TABLES

1.1 Densities of materials commonly used for membranes…..……...……...10

3.1 Theoretical resonant frequencies of membranes in a vacuum…….45

5.1 AVMI Model equations and variables…….76

LIST OF FIGURES

2.1 Engine configuration ……22

2.2 Silicon membrane fabrication……23

2.3 Photolithography mask to define membrane geometry……24

2.4 Generator fabrication process flow……25

2.5 Completed 3 mm membrane generator sitting on a dime……..25

2.6 Ring heater fabrication process……..26

2.7 Completed ring heater with membrane outlined……27

2.8 Engine assembly procedure……...29

2.9 Pulse system schematic……..30

2.10 TTL Circuit Diagram……31

2.11 Schematic of interferometer with assembled engine……33

2.12 Typical interferogram for 4 mm upper membrane assembled in engine……...33

2.13 Image of bubble and ring heater……34

2.14 Principle of operation of vibrometer……..35

3.1 Mass-spring-damper system……..37

3.2 Forced vibration mass-spring-damper system……...38

3.3 Free vibration response to an impact force……40

3.4 Forced vibration experimental schematic……..41

3.5 Frequency response of the forced vibration of a 3 mm generator engine……..43

3.6 Schematic of free vibration experimental setup……46

3.7 Free vibration “after-ringing” of 3 mm generator engine……..……47

3.8 Free vibration “after-ringing” of Si membrane engine……..……47

3.9 Comparison between forced vibration and free vibration……..48

3.10 Velocity response of an 4mm Si membrane engine to heat Pulse…….50

3.11 Curve-Fit of Free Vibration of Engine……...50

3.12 Repeatability of engine resonant frequency measured by free vibration..…….52

4.1 Schematic of engine……...53

4.2 Generator and Si membrane cross-section…….54

4.3 Free vibration experiment schematic…….55

4.4 Oxide mask for 4 mm silicon membranes…….57

4.5 Oxide masks for 6 mm and 7 and 8 mm silicon membranes…….58

4.6 Relative sizes of silicon membranes……..59

4.7 Semiconductor tape gasket dimensions…….59

4.8 Engine resonant frequency dependency on membrane side length…….……..60

4.9 Bubble diameter parameter……61

4.10 Large, medium, and small bubble assembles in engines……...62

4.11 Resonant frequency of 4 mm engine at varying bubble diameters…..……..63

4.12 Engine cavity depth parameter……...64

4.13 Effect of cavity depth on resonant frequency…….……...66

5.1 Non-dimensional parameter α as a function of bubble diameter……...70

5.2 Theoretical resonant frequency of silicon membranes versus side length..…...…71

5.3 Experimental resonant frequency as a function of bubble diameter……..72

5.4 AVMI factor Γ as a function of cavity depth……...……..73

5.5 AVMI Model fit for varying cavity depth ……74

5.6 AVMI Model fit for resonant frequency of various size engines……..75

5.7 AVMI Model for 500 Hz Operation……..78

CHAPTER 1

INTRODUCTION

1.1 MOTIVATION

Thermopneumatic membrane actuators have become increasingly important as a means of accomplishing work in various Micro-Electro-Mechanical Systems (MEMS) devices. Devices have been designed for flow control in valves [1,2] and micro pumps [3-7]. Thermopneumatic operation has proven to be an effective means for actuation in MEMS. Benefits of thermopneumatic operation include increased precision and control by use of resistance heaters, large displacements of actuator components, as well as relatively simple actuator components, often consisting of only a heat source, pressure cavity, and membrane or diaphragm. However, the entirety of micro thermopneumatic actuators are limited to operate at low frequencies due to the rate at which heat can be added and, more critically, removed from the system. This limits most devices from operating at resonant frequencies where added benefits can occur. Resonant frequency can result in lower power consumption, increased displacements, and higher conversion efficiencies. Even more promising, it may be possible that a thermopneumatic actuator operating at resonant frequency can actually result in a four-stroke thermodynamic cycle creating an engine [8] or refrigeration [9] device.

If actuators are to achieve the benefits of operating at resonant conditions, they must overcome the constraints composed by insufficient heat transfer. In this regard, resonant frequency can be achieved if the rate of heat transfer is increased to system resonant frequency or if the systems parameters are changed to lower the system resonant frequency for operation at adequate heat transfer rates. Ideally, by increasing both the

heat transfer rate and controlling the system resonant frequency an optimal operation frequency can be attained. A vast amount of research has been performed to implement means for increasing heat transfer including heat pipes [10,11] and thermal switches [12,13]. However, there is relatively little being done in thermopneumatic actuators to control resonant frequency by changing system parameters. More commonly, researchers have settled for sub-resonant frequency operation or have ruled out thermopneumatic operation as a means of achieving resonant frequency, relying on other means of actuation, such as, piezoelectric or electrostatic.

A novel MEMS thermodynamic engine is in development by researchers at WSU. The engine consists of a piezoelectric thin film deposited on a flexible silicon membrane encapsulating a two-phase liquid vapor mixture. When the fluid is alternately heated and cooled, changes in cavity pressure result in the strain of the piezoelectric membrane. Strain induced within the piezoelectric is converted to an electric charge across electrodes that can be harvested. In this manner, pulsed heat is converted to mechanical work through the expansion of the membrane, and mechanical work is converted to electrical work through the piezoelectric phenomena [14]. Heat rejection has been defined as a limiting parameter to resonant frequency operation [15], however, an effective means of control remains under development. Therefore, this work shall investigate system parameters as a means to control resonant frequency operation regardless of the heat transfer rate. Since the engine is essentially a thermopneumatic actuator, this work will benefit the field of thermopneumatic actuators as a whole.

1.2 LITERATURE REVIEW

1.2.1 Membrane Resonators

The goal of this review is to explore the methods used to achieve specific operating resonant frequencies for MEMS devices employing membranes. Specifically, the parameters affecting the resonant frequency of a membrane coupled to a two-phase fluid-filled cavity, operating as an engine, shall be investigated.

The use of resonating membranes in thermopneumatic actuators in the literature is to date virtually nonexistent. This is most likely a product of relatively low heat transfer rates. However, the advantage of thermopneumatic actuation over other methods currently employed merits the investigation of ways to operate membrane resonating actuators with pulsed heat. Thermopneumatic operation often requires less power, can provide greater displacements, and devices often undergo fewer processing steps than the more common actuation methods. The majority of resonating actuation devices employ piezoelectric or electrostatic actuation. Although these actuators are well suited for very high frequency operation, they often require very high voltages in the hundreds to thousands of volts for minimal membrane displacements, making them unpractical for many MEMS devices.

The lack of resonating thermopneumatic actuators in the literature requires one to explore other avenues where resonating membranes are used, in order to design a means of controlling the resonant frequency of a thermopneumatic engine. Fortunately, devices incorporating resonating membranes are frequently used in MEMS, including micro pumps [16-18], Micro Ultrasonic Transducers [19-21], pressure sensors [22,23], and even a micro cryogenic cooler [9]. In each of these systems, controlling resonant frequency is

of utmost importance. Micro pumps operating at resonant frequency have higher flow rates, increasing possible applications and reducing power requirements. MUTs are able to detect and transmit signals at specific frequencies, effectively filtering noise from other frequencies. Accelerometers and pressure sensors measure changes within environments proportional to fluctuations in their respective natural frequencies. The micro cryogenic cooler relies on resonant frequency to achieve compression and expansion vital to its operation [9]. In each case, it is important to be able to control or tune the effective resonant frequency of the system in order to achieve the desired operation. The parameters used to tune the natural frequency of each device are the geometry, material properties, surrounding fluids, and packaging. Altering these parameters changes the mass, stiffness, and damping properties, all of which define the resonating system. Designing a resonating system requires knowledge of all factors involved.

In order to fully characterize a resonating system it is beneficial to observe how the additions of individual parameters influence resonant frequency. As an example, a membrane micro-pump can be divided into a series of components, with each components addition affecting the overall system. Bardell *et al.* showed the advantage of this when they analyzed the resonant frequency of a resonating micro-pump [24]. First, they analyzed the contribution of the membrane on resonant frequency frequency. Then the fluid effects were added to the membrane. Finally, the contribution of the valves and cavity were coupled to the membrane and fluid. This approach provided a systematic method to understand the contribution of each component on the resonating system. In the same way, the membrane engine under consideration in this present research can be divided into three components, the membrane generator, the working fluid, and the

engine cavity, each influencing resonant frequency independently. The following review will explore resonant systems with only the membrane, the coupled membrane and fluid system, and finally the coupled membrane, fluid, and cavity.

1.2.2 Membrane Effects

A membrane is defined as a perfectly flexible two-dimensional plane of zero thickness held in tension by a force so great that deflections cause no change in the membrane tension [25]. The vibration characteristics, and thus, resonant frequency, are almost entirely dependent upon geometry and material properties. Membrane geometry is specified by shape, size, thickness, and cross-section. The material properties influencing resonant frequency include the density, residual or internal stress, elastic modulus, and Poisson's ratio.

In theory the vibration of an ideal membrane is quite simple to model. Textbooks readily give equations of motion for vibrating membranes of various shapes and sizes. However, the inherent assumptions to linear vibration rarely hold for real-world applications. Although it provides a decent guide of what factors will influence vibration, the assumption of linear membrane vibration fails under a generally accepted "rule-of-thumb" of deflection amplitudes on the order of the membrane thickness [26]. Recent research has shown that even this estimate is far too liberal and non-linear effects can be observed at vibration amplitudes smaller than four percent of the membrane thickness [27].

Many researchers are now developing models to explain non-linear effects in membranes by viewing them as plates subject to bending and internal stresses. One such

study develops a model for the non-linear free vibrations of rectangular plates with a combination of clamped and simply supported boundary conditions [28]. The clamped conditions yield higher resonant frequencies than the simply supported boundary conditions traditionally used for membrane analysis. Also, model results show that vibration amplitudes on order of the thickness can result in a thirty-five percent increase in fundamental resonant frequency frequency.

Taking these considerations into account, and the fact that most membrane actuators running at resonant frequency do so in an effort to achieve maximum displacements, non-linear effects must be considered. The task of modeling non-linear membrane vibration has been pursued by many research groups [28,29]. However, studies coupling non-linear membrane vibration to complete resonating systems are still fairly scarce in the literature. More often non-linear effects in systems are ignored, attributed as sources for error, or vibration is limited to the linear regime. Many other resonant frequency applications, with large amplitude membrane vibration, opt to experimentally determine vibrating characteristics, as the modeling of such systems is forbiddingly difficult [30-32].

A review of the literature shows that membrane shape is dictated less by the specific application and more so by the methods available for fabrication. The most common membrane shape in devices is the square, or rectangular membrane. Rectangular membranes are easily fabricated using the anisotropic selectivity of wet enchants such as KOH, TMAH, or EDP [33]. The typical process flows for creating rectangular membranes employing either a boron or Si_xN_x etch stop are detailed in [33]. Circular membranes, or virtually any shaped membrane, are created in silicon by reactive

ion etching (RIE) or deep reactive ion etching (DRIE). A study by Arik *et al.* presented the analysis of square, rectangular, circular, and elliptical membranes fabricated through RIE [34]. The process flow for creating circular membranes is detailed in [33]. Although RIE and DRIE provide flexibility in membrane shape and the possibility of etching vertical sidewalls, the initial equipment cost is extremely expensive. Therefore, it is typically used only when available or for applications where the membrane shape is critical.

Provided access to the appropriate fabrication equipment is available, specific shapes may offer advantages for the specific resonant frequency requirements of various applications. Resonant frequency is influenced by a shape factor or natural frequency parameter, often given by the symbol λ_{ij} [35], where i and j specify the mode of vibration. From the fundamental equations for membrane resonant frequency, it can be shown that the frequency of the fundamental mode of a rectangle is higher than that of a square with the same surface area, and the first mode of a circle is roughly ninety-five percent that of a square [35].

Membrane size is the primary method of controlling resonant frequency in MEMS applications. This is so evident in literature that it is often the membrane size that dictates its applications. The smallest membranes used in MEMS are as small as 40 μm [19]. They, and membranes with side lengths or diameters up to about 1 mm, are primarily used for the sending and receiving of ultrasonic signals [20]. Larger membranes are better suited for resonant frequency applications requiring large deflections such as micropumps [7], droplet ejectors [36], or speakers and microphones operating in the audible range [32,37].

The theories dictating membrane size effects on resonant frequency have long been known, going back to Lord Rayleigh and his studies of sound. In 1877 Rayleigh published his works on the theory of sound, where he showed theoretically and experimentally the relationship between size and shape on membrane natural frequency [25]. He showed that the natural frequency, or pitch, of a membrane increased as side length decreased. Likewise, changing the shorter length of a rectangular membrane has a larger effect on pitch than altering the longer side length.

The resonant frequency of a membrane can also be tailored by changing the membrane thickness. This effect was observed in a study by Paneva and Gotchev [27]. They tested square silicon membranes with 5.35 mm side lengths. Membrane thickness was varied by etch stop doping levels and anisotropic etching in KOH, yielding membranes with 5.9, 7.5, 10.4, and 15 μm thickness. The membranes were then driven to resonant frequency by an AC-voltage applied to a thin film piezoelectric structure processed on the membranes. Results showed that the resonant frequency of the first mode decreased proportional to the negative 0.45 power of the thickness. The resonant frequency of an ideal membrane decreases proportional to the negative ½ power of the thickness. The difference is reported as being due to the stiffness of the structure.

Muralt *et al.* also observed the deviation of resonant frequency behavior from a pure membrane due to thickness [38]. They used a 2 mm diameter membrane and varied the silicon thickness from about 2 μm to 23 μm. The membranes were then excited to resonant frequency using a piezoelectric composite layer processed on the center of the membranes. Results showed that membranes with a silicon thickness below about 3 μm displayed a resonant frequency decrease with proportionality near that of a pure

membrane, that is, $f \propto (\text{thickness})^{-1/2}$. As the Si thickness was increased to about 7um, the resonant frequency increased proportional to the thickness, exhibiting the behavior of a clamped disk or plate. The point at which the membrane underwent the transition from membrane behavior to plate behavior is stated as being dependent on the tension of the membrane. In this way a membrane with small tension forces requires a thinner thickness to produce a plate-like response. Although a particular value for tension of the membrane was not given, this may explain what seems like inconsistencies between this study and the one by Paneva *et al.* [27] discussed earlier.

Similar to increasing membrane thickness, many MEMS devices employ the use of bosses, or proof masses, by selectively leaving a mass of silicon with a much thicker cross section than that of the surrounding membrane. This method is most common in devices requiring greater sensitivity to inertial changes, such as accelerometers and vibration sensors. Thomas developed one such device as vibration sensor for tool monitoring [39]. The vibration sensor employed a bossed membrane as a seismic mass in order to increase the sensitivity of the sensor. He found that a membrane with a central boss operating at the same resonant frequency as a membrane with a uniform cross-section resulted in an order of magnitude increase in sensitivity measuring much smaller accelerations.

Another device using a bossed membrane is McEntee and Bowman's design for a miniature Sterling cycle cryocooler, which required a membrane with sufficient inertia while operating at resonant frequency to achieve a thermodynamic cycle necessary for cooling [9]. Unable to achieve this with a membrane of uniform thickness operating at a specific frequency, they employed a membrane with a thicker bossed center surrounded

by a thin, more flexible membrane. Although the authors have to date failed to present the operation of a micro cryocooler, they developed a model validating experiments to create an optimal membrane with the largest kinetic energy developed for a particular swept volume. This optimum was achieved with a circular boss twenty times thicker than the surrounding membrane, with a radius 30% that of the entire membrane structure. One shortcoming of the study was that the authors intentionally restricted the membrane deflection to the linear regime in order to make the model easier to solve. In doing so, they eliminated possible compression and expansion benefits to their application that may have resulted from larger membrane deflections.

In most cases defining the geometry of a membrane directly changes the mass of the system. The material used to fabricate the membrane also has an effect on the system mass and natural frequency. The densities of some of the most common materials used for membranes in MEMS are shown in Table 1.1. Because the majority of membranes are actually composites including layers to sense and actuate membrane vibration, the densities of other common materials are included in the table. However, density is not

Material	**Young's Modulus (GPa)**	**Density (g/cm^3)**
Silicon	~ 190	2.3
SiO_2	~ 70	2.66
Silicon Nitride, Si_3N_4	~ 130	3.44
Gold	80	19.4
Platinum	147	21.4

Table 1.1 Young's Modulus and densities for materials commonly used in membrane structures [33].

the only means in which material properties will influence the resonant frequency of a membrane. The Young's Modulus, Poisson's ratio, and the residual stress (related to the material and processing) will also have a large contribution.

The stiffness of oscillating systems is most often thought of as the spring constant of the system. The system spring constant is equal to the force required to produce a unit of linear deflection. Likewise, in an ideal membrane the stiffness is accounted for by the tension of the membrane per unit length of the edge [35]. As previously mentioned, the pure membrane includes no bending effects of the structure, as by definition it has no thickness with which to resist bending. The stiffness of a plate, however, is highly dependent upon bending moments and therefore depends on both the elastic modulus and Poisson's ratio. Muralt *et al.* showed that a realized MEMS fabricated membrane may exist somewhere between a pure membrane and a plate, the degree of either dependent upon the tension in the membrane and its thickness [38]. A membrane with a large thickness and small in-plane tension will behave more like a plate, however, a membrane with very large in plane-tension will behave more like a pure membrane.

Degen *et al.* showed that the dependence of resonant frequency on in-plane tension could be used to determine the residual stress of membranes used for open stencil masks and mini-reticles [40]. In their study silicon membranes with a side length of 6 mm and a thickness of 6 μm were evaluated. Membranes were excited by pressure waves from a speaker placed in close proximity to the membrane. A piezo-resistive cantilever was placed in contact with the center of each membrane in order to measure the amplitude response to the sound waves. The maximum amplitude during a frequency sweep defined the position of the first resonant mode. Once the resonant frequency was

known and accommodations were taken for air loading effects, the residual stress was calculated from:

$$f_{11} = \frac{1}{2}\sqrt{\frac{2 \cdot \sigma_0}{\rho \cdot L^2}} \qquad 1.1$$

with: f_{11}: first resonant mode of vibration

σ_0: residual stress

ρ: membrane material density

L: membrane side length

Calculated residual stresses from resonant frequency measurements agreed within 0.1 MPa of other methods employed. The results validate the resonant frequency method for determining residual stress. Likewise, they show how changing the residual stress of membranes is an effective means of tuning resonant frequency.

As discussed earlier, most membranes used as sensors and actuators are actually laminates of various layers. These layers also individually contribute to the overall residual stress of the membrane, as noted by Kennedy *et al.* [41]. Employing a fairly common piezoelectric composite structure on a silicon membrane substrate, Kennedy measured the residual stress contributions from each deposited layer. The layered structure consisted of a silicon membrane, TiW, Pt, PZT, and Au. The residual stress of each individual layer was measured using x-ray diffraction. Each layer contributed to the composite residual stress measured by the bulge test method in which the membrane is pressurized on one side and deflection measurements are taken. The goal was to reduce the overall residual stress in the composite. To accomplish their goal they added an additional tungsten compressive layer, effectively lowering the composite tensile residual

stress. In this manner, the resonant frequency of a 3 mm square membrane with a composite thickness of about 2.8 μm was reduced from 23 kHz without a compressive layer, to 18 kHz with the addition of a compressive layer.

Most composite membranes are designed for sensing or actuation and therefore undergo mechanical and electrical couplings that can shift the resonant frequency. Although this particular topic is beyond the scope of this review to investigate in detail, it is interesting to note the methods that piezoelectric and electrostatic resonators can employ to electrically effect resonant frequency. Specifically, a resistive or capacitive load placed across the electrodes of a piezoelectric transducer can result in a small shift of the first mode [42]. Similarly, the resonant frequency of electrostatic transducers can be precisely tuned through the addition of a DC-bias [43].

1.2.3 Membrane – Fluid Effects

The media or fluid surrounding a resonating structure has a dramatic effect on the system adding mass, damping, and in the case of a compressible fluid, spring forces. Although these effects have been observed and theoretically explored for more than a century, a broad range of research groups today continue to explore resonating structures and fluid interactions. In the area of membranes, research has been limited to structures either surrounded completely by a homogeneous fluid or having one side exposed to a homogeneous fluid. However, the area of MEMS thermopneumatic membrane actuators and engines provides a unique situation in which a two-phase fluid is in contact with the vibrating structure. In fact, only one study was found that addressed the problem of a vibrating structure in a two-phase fluid. Billingham attempted to model the effect of a two-phase fluid in contact with an idealized resonating rod [44]. He found that a two-

phase mixture with fluids of similar density, such as oil and water, could be approximated as a single-phase fluid with a weighted density. However, his single-phase model failed when he considered a two-phase mixture of fluids with vastly different densities, such as water and air. Fortunately, homogeneous fluid studies provide a firm foundation upon which to build for the case of a two-phase fluid and can provide very good qualitative trends in fluid properties influencing resonant frequency. The primary fluid properties of interest are viscosity, density and pressure.

Damping, largely due to viscous forces in phase with the velocity of the structure, has very little impact on resonant frequency for fluids with viscosities less than 0.006 $N \cdot s/m^2$ [45]. For reference, at room temperature water has a viscosity of about 0.001 $N \cdot s/m^2$ and air has a viscosity of 0.000018 $N \cdot s/m^2$ [46]. More practically, the viscosity serves to dissipate system energy, causing a faster decay in free vibration and reducing the resonant frequency amplitude at forced vibration. Inaba *et al.* showed that the amplitude of the resonant frequency peak within the frequency response of a cantilever decreased and the half power width broadened with higher viscosity fluids, but the shift in resonant frequency due to viscosity was negligible [47].

Physically, a shift in resonant frequency in most fluid media is due to added mass effects, where the inertia of the fluid moving in phase with the displacement of the vibrating structure acts as an effective added mass to the structure itself. Lamb pioneered the theories behind this phenomenon in 1921 as a method to answer questions arising within submarine signaling [48]. Lamb clamped a circular elastic plate within an aperture of a solid rigid wall. One side of the plate and wall were then placed in contact with water. His results showed that the natural frequency of the plate with one side in

contact with fluid could be related to the natural frequency of the plate in a vacuum by a multiplied factor proportional to the kinetic energy of the plate and the kinetic energy of the fluid. The relationship between the kinetic energies of the plate and fluid are still used extensively by researchers to theoretically determine added mass effects on resonating structures in fluid.

Since Lamb's research, the ratio between the kinetic energy of the fluid due to plate or membrane motion and the kinetic energy of the plate itself has been known as the added virtual mass incremental factor, or AVMI factor for short [49]. The AVMI method provides a very powerful analytical approach to approximating the effect of fluid loading on vibrating structures. Kwak and Kim showed how the AVMI factor could be used to accurately predict the resonant frequency of a circular plate under various clamping conditions [49]. They showed that the AVMI factor, β, could be solved simply as:

$$\beta = \frac{\rho_f}{\rho_P} \cdot \frac{r_P}{t_P} \cdot \Gamma \qquad 1.2$$

with: ρ_f: fluid density

ρ_P: plate density

ρ_P: plate radius

t: plate thickness

Γ: non-dimensional AVMI factor accounting for vibration mode and clamping

This same method was later employed by Kwak to solve for the resonant frequencies of circular membranes in contact with fluid under various clamping conditions [50]. The AVMI method has been well accepted by many other researches as a method to

accurately predict the resonant frequencies of plates and membranes in contact and submerged in both compressible and non-compressible fluids [35,40,45,51-54].

An exact solution to the fluid-membrane coupling has not been completely determined. The solution becomes extremely difficult because although the membrane solution is two-dimensional, the fluid movement is three-dimensional, adding to its complexity. Structural-fluid interactions as a whole have received a lot of attention to determine exact solutions, but as structure shapes become more complex, the amount of available research becomes limited. For example, the vibration of a beam or cantilever in a fluid has been well explored numerically [55,56,57], but an exact solution to a membrane in contact with fluid is, to date, unavailable. For cantilevers it is common to use the Navier-Stokes equations to determine fluid reaction forces [58]. In the area of plates, the Analytical-Ritz method [59] has been employed, as well as the Finite Element Method [60].

The largest application area of MEMS membrane-fluid systems operating at resonant frequency is micro-pump systems. The effect of the fluid-structure interaction on resonant frequency is commonly determined by observing the effect of operating frequency on pump flow rate [30]. The operating frequency resulting in the greatest flow rate defines resonant frequency. When modeling micro-pumps the most common approach is to determine the added mass to the resonating system by solving equations for the flow-rate per cycle [17,61,62]. In the same way, system damping is determined by resistance flow through the inlet and outlet valves. Although the theory of determining added mass in micro-pumps sounds quite simple, the actual calculations are

quite rigorous, as the majority of MEMS pumps developed today use nozzles and diffusers to direct flow [16,17,24,62] resulting in coupled non-linear equations [62].

Another common use for resonating membranes is in the area of pressure sensors. An increase in pressure results in an increase in the surrounding fluid density. As noted earlier, an increase in density adds mass to the system resulting in a decrease in resonant frequency. However, the influence of pressure alone is quite small. Most research showing this effect has been performed on cantilevers surrounded by fluid. Inaba and Han showed the effect of changes in pressure at low pressures between 10 and 100 kPa, which resulted in a maximum frequency shift of only about 0.2% [63]. In another study Mertens *et al.* tested cantilevers over a range of pressures from 0.01 Pa to 1000 kPa, and observed a maximum frequency shift of just 2.5%, 2.3% of which occurred at pressures greater than 100kPa [64]. Since the influence of pressure on resonant frequency is quite small, virtually all resonating membrane pressure sensors rely on a pressure differential across each side of the membrane, resulting in changes in deflection. In this scenario a rise in pressure on one side of the membrane results in an increase in resonant frequency due to membrane stiffening. Defay *et al.* showed that this effect could be used to measure pressure with very high precision, with a resolution of 11.5Hz/kPa in the 2 to 10 kPa range [22]. Keeping this in mind, it is very important to control the mean pressure differential across the membrane, as the impact on resonant frequency can be quite large.

Up to this point, the compressibility of the working fluid has been neglected, which is common for most systems operating in a fluid infinite in all directions. However, the packaging of Microsystems allows for sealed cavities in which fluid can act as a spring. Also, it stands to reason that the cavity dimensions may cause further effects

on the resonant frequency due to the properties of the working fluid. Therefore, in the following section, the effects of a membrane encapsulating a fluid in a cavity with rigid sidewalls shall be explored.

1.2.4 Membrane – Fluid – Cavity Effects

The first and most obvious effect of a membrane sealing a compressible fluid within a cavity is the opportunity for the membrane deflection to generate pressure within the cavity. In this way the membrane-cavity system is analogous to a simple free-piston and closed cylinder. The piston-cylinder problem is readily available in textbooks and in its ideal form behaves as a mass-spring system. The mass of the system is equivalent to the mass of the piston and the compressible fluid is modeled as a one-dimensional spring. Assuming the system is isentropic, the effective spring constant of the compressible fluid is then, $k = \kappa p_0 A^2/V_0$, where A is the piston area, p_0 is the mean pressure, V_0 is the cavity volume, and κ is the non-dimensional polytropic constant related to the ability of the volume to transfer heat (for air $1 \leq \kappa \leq 1.4$) [35]. The cavity dimensions, therefore, have the potential to stiffen the membrane system resulting in an increase in resonant frequency.

Another stiffening effect can be observed in unique situations when the vibrating structure, in liquid, is very near to a solid wall, experimentally $< 5\mu m$ [65]. The surface tension of a fluid can then result in two force contributions. First is the capillary-type force effect, where the surface tension force acts tangential to the meniscus of the fluid. For an enclosed membrane, this force has very small effects, whereas a cantilever or plate with free edges may allow the meniscus to extend to the sides of the structure, resulting

in a force normal to the width of the structure. Abe *et al.* noted this effect when studying the effects of stiction in micro cantilevers [66]. The second force contribution is defined as Laplace pressure, and reacts normal to the width of the structure and rigid base. This force was shown to act as a spring by Lai and Fang as it is proportional to the inverse of the distance between a vibrating micro cantilever and a rigid base [65]. Further, the spring constant and the damping coefficient, due to surface tension, were shown to be proportional to the inverse of the gap squared and the gap cubed, respectively. This effect has not been observed in membrane or plate systems most likely because devices operating in liquids have yet to reach the scale of having a large surface area relative to a gap height less than 5μm.

Some research has been performed on cantilevers and plates oscillating in a fluid normal to a solid surface that can give insight into the membrane-fluid-cavity interaction. Naik *et al.* showed that the resonant frequency of a cantilever in liquid was dependent upon the ratio of the gap between the lower side of a micro cantilever and a rigid base and the cantilever width [58]. Their test apparatus consisted of a piezoelectric actuated cantilever clamped on one end and enclosed within a cavity containing a liquid. All walls of the cavity were rigid during testing with the top of the cavity 4 mm above the cantilever and the floor of the cavity adjustable to vary its distance from the cantilever, defining the gap height. The top plate of the cavity was vented in order to maintain pressure and allow adjustment of the gap height. The gap height was varied from 2 mm (gap height/cantilever width = 2) to 1 μm (gap height/cantilever width = 0.001). Gap heights greater than 1 mm showed very small shifts in resonant frequency and could be considered consistent with the condition of an infinite media. However, a gap height of 1

mm resulted in a decrease in first mode resonant frequency of 50%. The authors attributed the decrease in resonant frequency to an increase in added mass on the cantilever as gap height decreased. They also showed that the added mass effect resulted from changes in the pressure field normal to the surface of the cantilever.

In another study, Kwak and Han showed the effect of fluid depth on a free-edge circular plate in contact with fluid [67]. The fluid gap between a steel plate with a radius of 15 cm and a thickness of 0.2 cm and a rigid bottom was varied from 15 cm to 1 cm. The AVMI method discussed earlier was employed to model the effect of the fluid inertia with an additional non-dimensional added virtual mass incremental (NAVMI) factor to account for mode shape, clamping conditions, and depth contributions. As the name of the method suggests, Kwak and Han came to the same conclusion as that of Naik *et al.* [58] that a decrease in gap height results in added mass to the system, and a subsequent decrease in resonant frequency.

1.3 RESEARCH OBJECTIVES

The primary objectives of this research are to design an experiment to measure the resonant frequency of an assembled membrane engine, measure the effects of engine parameters on resonant frequency, and finally, to develop a simplified model to extrapolate resonant frequency based on specific engine configurations. The success in meeting research objectives will be assessed by the ability to assemble and measure an engine configuration with a resonant frequency below 500 Hz.

Designing a resonant frequency experiment requires determining the correct means to actuate and measure the response of the upper membrane of the engine at

specific frequencies. The actuation methods available fit into two categories of forced vibration or free vibration. The primary goal of the experimental design is to determine a method that will allow for repeatable measurements in a simple set up with the flexibility to measure different engine configurations.

The parameters defining the engine configuration are the membrane, working fluid, and cavity. In order to determine the influence of each parameter on resonant frequency, methods must be developed or expanded from present capabilities to assemble engines under various controlled configurations. Measuring the resonant frequency of various configurations will yield a relationship between individual engine parameters and engine resonant frequency.

Once experimentation is complete, a model will be developed to quantitatively predict the first resonant mode of an engine based on a set of given parameters. The model will be a simple analytical approach with experimental measurements made to calculate specific constants. The primary goal of the model in not to achieve an exact solution to the membrane, fluid, and cavity coupling, as it is beyond the scope of this project, rather the final product will provide trends to assist in an effective membrane micro engine design.

CHAPTER 2

FABRICATION AND EQUIPMENT

2.1 ENGINE FABRICATION

P3 Engine components are fabricated in-house at the WSU Center for Materials Research Clean Room Facility. A single engine consists of an upper piezoelectric laminate membrane, a sealed cavity containing a two-phase fluid, and a lower, smaller membrane with a resistance heater facilitating heat transfer into the cavity. A schematic of the device is shown in Figure 2.1. Components are batch fabricated on three-inch double-sided <100>-oriented silicon wafers. This section will cover the basic process flow for a membrane generator and heater, as well as a detailed look at the engine assembly. A detailed process outline including recipes can be found in reference [68].

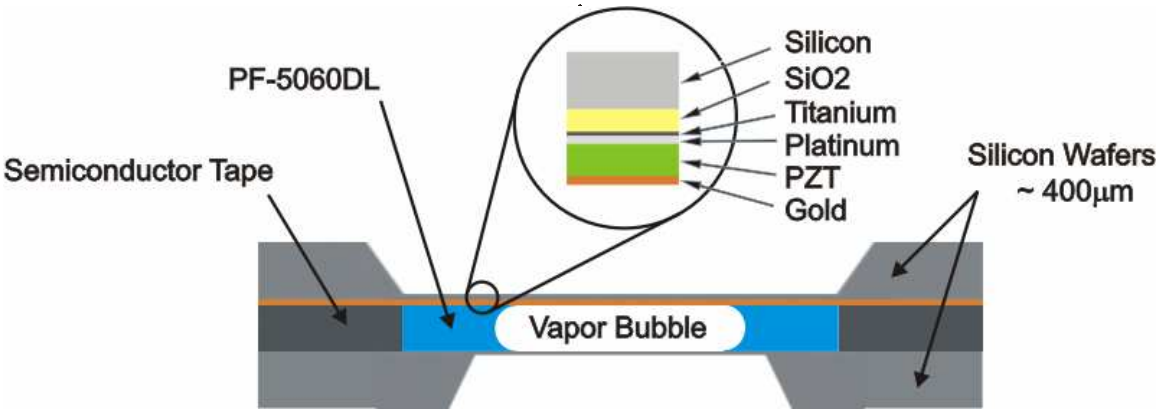

Figure 2.1: Engine configuration including upper membrane generator, cavity defined by semiconductor tape gasket, and lower heater membrane [15].

2.1.1 Membrane Fabrication

The membrane generator and heater are both fabricated on bare silicon membranes, for which the processing steps are the same. Also, it may sometimes be advantageous to replace the generator membrane with a bare silicon membrane. Therefore, the fabrication of bare silicon membranes will be covered first. The process flow for silicon membranes is shown in Figure 2.2.

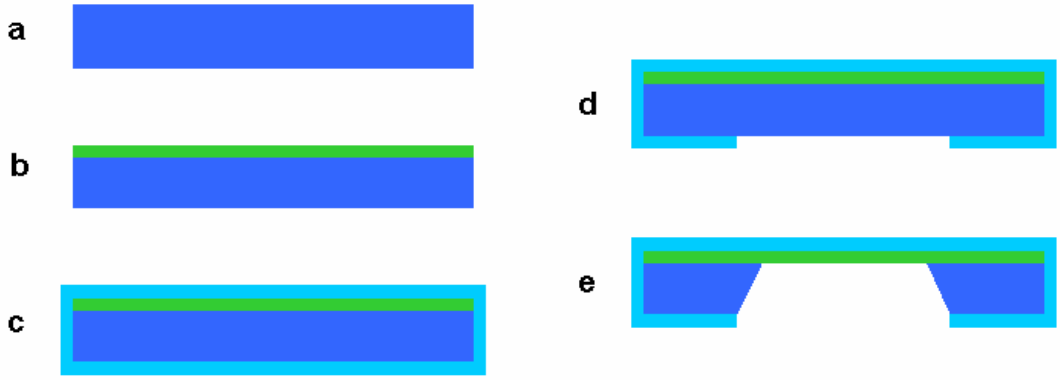

Figure 2.2: Silicon membrane fabrication (a) bare Si wafer (b) boron doping (c) oxide growth, (d) pattern oxide, and (e) anisotropic etch in EDP.

Membrane fabrication begins with a three-inch p-doped (100)-oriented double-side polished wafer. The native oxide is stripped in Buffered Oxide Etch (BOE) and a high temperature wet oxide is grown in a furnace. One side of the oxide is then stripped and boron is diffused into the surface. The boron doped silicon layer will later act as an etch stop. The remaining oxide is then stripped from the wafer and a more uniform low-temperature oxide is grown to 100 nm. The oxide layer on the non-boron doped side is then patterned using photolithography and a Buffered Oxide Etch. A typical oxide mask for creating 3 mm side length membranes is shown in Figure 2.3. The oxide mask serves to define the membrane geometry. Wafers are then placed in an Ethelynediamine

pyrocatechol (EDP) bath to create membranes. EDP is an anisotropic wet etchant that shows a preferential etch rate in the (100) direction [33]. The boron doping completed earlier serves as an etch-stop to EDP and defines the membrane thickness. Following cleaning, wafers are now ready to proceed to generator or heater fabrication.

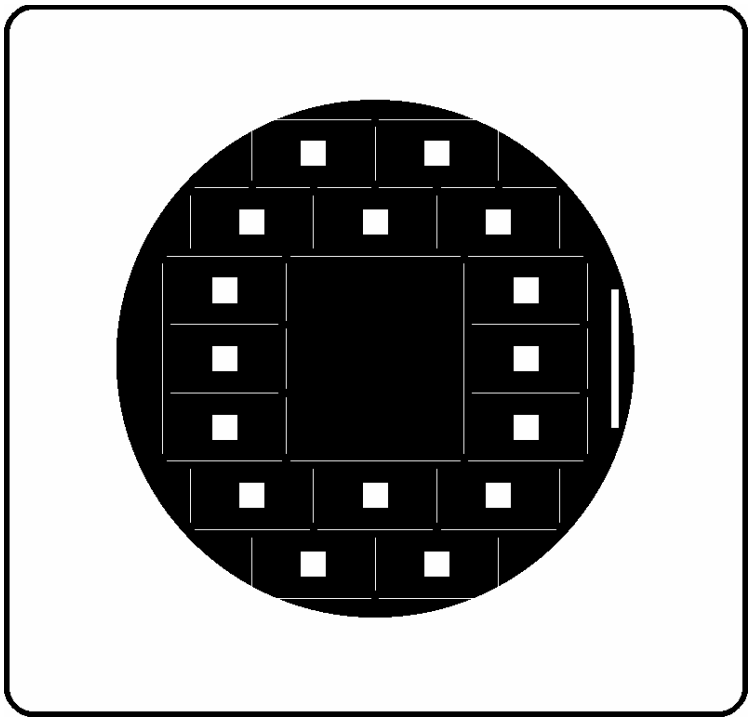

Figure 2.3: Photolithography mask to define membrane geometry for 3 mm membranes.

2.1.2 The Membrane Generator

The process flow for generator fabrication following membrane fabrication is shown in Figure 2.4. Generator processing begins with deposition of a 12.5 nm TiW and 175 nm platinum bottom electrode using DC-Magnetron sputtering. The piezoelectric ceramic lead-zirconate-titanate (PZT) is then spun on the wafer in a sol-gel process. Next, 75 nm TiW and 300 nm gold films are sputtered on the PZT layer and the gold and

TiW are patterned to define the upper electrode. Finally, PZT is patterned and removed in high stress areas on the membrane to provide greater compliance, and the wafer is broken up into individual die. A completed membrane generator die is shown sitting on a dime in Figure 2.5.

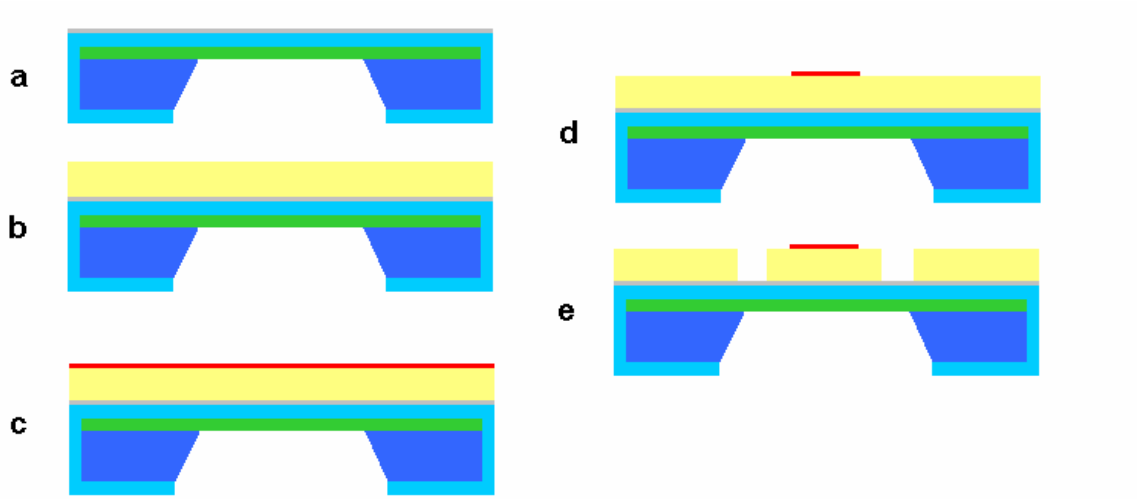

Figure 2.4: Generator fabrication process flow (a) platinum bottom electrode deposited, (b) PZT deposited using Sol-gel process, (c) gold top electrode deposited, (d) top electrode patterned, and (e) PZT patterned to relieve high stress regions and access to bottom electrode.

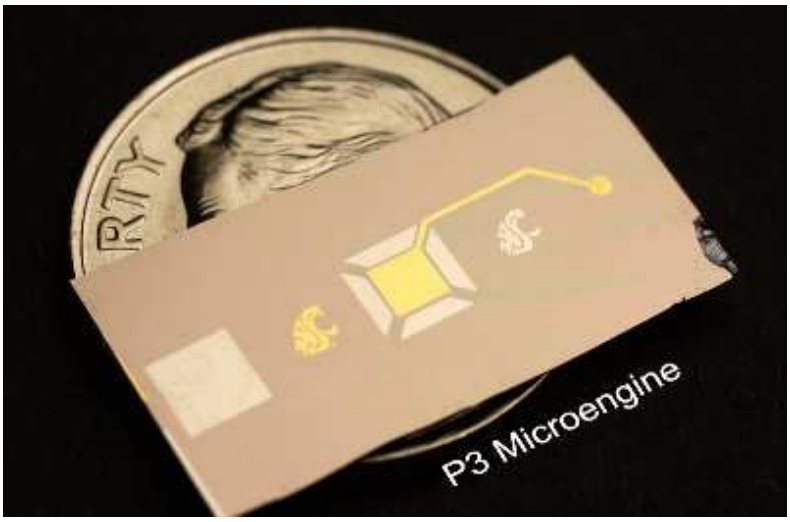

Figure 2.5: Completed 3 mm membrane generator sitting on a dime [15].

2.1.3 Heater Fabrication

Heater fabrication following membrane fabrication is shown in Figure 2.6. The only difference between heater and generator processing is the mask used to define the geometry of the heater membrane, as heater membranes are traditionally smaller than generator membranes. This provides greater deflections to the membrane generator when assembled in an engine. Following the anisotropic EDP etch, 75 nm of TiW and 300 nm of gold are deposited onto the membrane side of the wafer. The gold and TiW are then patterned and removed through photolithography to define electrodes and resistance ring heaters in the center of the membranes. Finally, the wafer is diced into individual die. A typical heater die is 10 mm by 18 mm and contains a 2 mm square membrane with a 1.8 mm diameter ring heater. A completed ring heater is shown in Figure 2.7.

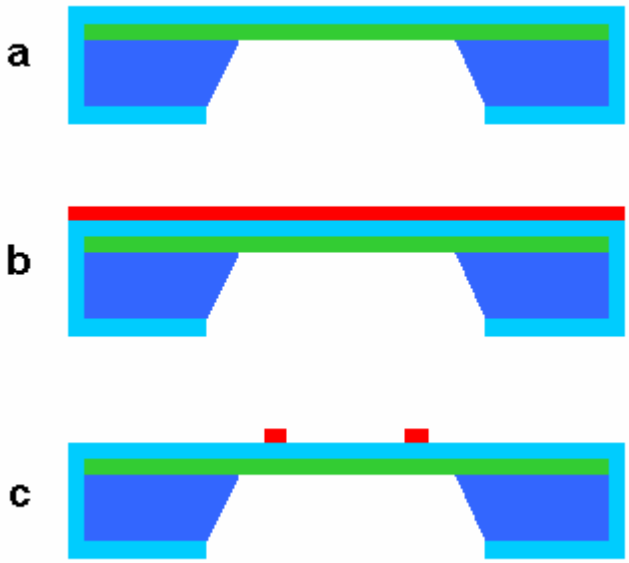

Figure 2.6: Ring heater fabrication process (a) bare silicon membrane with oxide, (b) gold deposited, and (c) gold patterned to define resistance ring heater and electrodes.

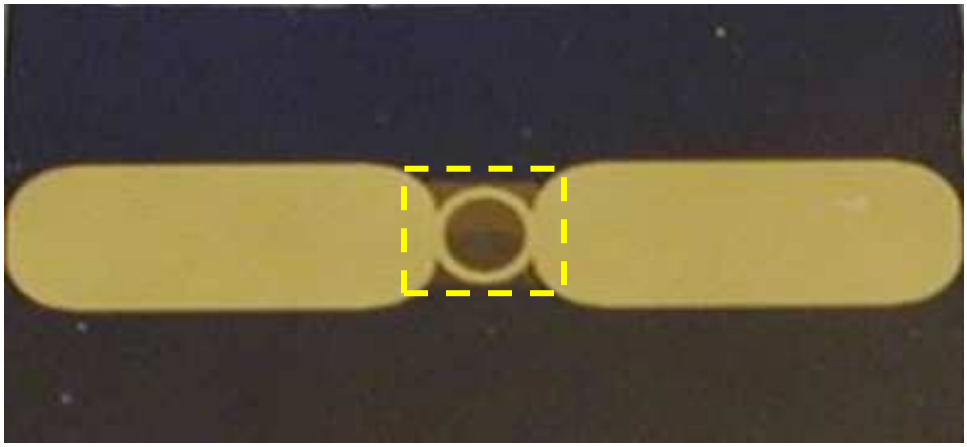

Figure 2.7: Completed ring heater with membrane outlined.

2.1.4 Engine Assembly

Once heater and generator die are complete they can be assembled into a single engine. Engines are currently assembled by hand, and held together through the clamping pressure of an acrylic carrier. The acrylic carrier is clamped together with four screws and provides access to generator and heater electrodes and visual access to the membranes themselves. Figure 2.8 shows the process of assembling a single engine. (1) First an individual heater die is centered on the lower carrier plate. (2) Next a gasket is cut from semiconductor tape and attached to the heater, ensuring that no air bubbles are trapped under the gasket. A single layer of semiconductor tape is 75 μm thick. Multiple layers of tape can be used to tailor the cavity depth. The inner square of the gasket is 2 mm larger than that of the generator membrane and the outer dimension is at least 4 mm larger than the inner, in order to provide a sufficient sealing surface. (3) The working fluid, PF-5060, a specialty refrigerant from 3M®, is then flooded into the engine cavity using a syringe. As the cavity is being flooded, the membrane generator, or upper membrane, is placed membrane side down onto the cavity. (4) Next, the upper membrane is centered over the heater and cavity by sliding it into place. A bubble is usually generated at this point due to air entrapped within the cavity. Some attempt can

also be made at controlling the amount of air trapped in the engine by sliding the upper membrane in such a way as to expose a corner of the cavity. Bubble size is then determined by how long the fluid in the cavity is allowed to evaporate. After an appropriate amount of time, the membrane generator can then be slid back into its central position. (5) An o-ring is then placed on the backside of the membrane generator to provide even pressure to the device stack. (6) Finally, the upper acrylic carrier plate is centered above the engine on the engine and clamped down using four screws, one at each corner of the carrier. This must be done with care, because the generator membrane tends to bulge out as the carrier applies pressure through the o-ring. The ideal assembly results in the generator membrane having a flat to very slightly positive initial deflection. With experience and patience, engines can be assembled with repeatability at initial deflections between zero and ten micrometers.

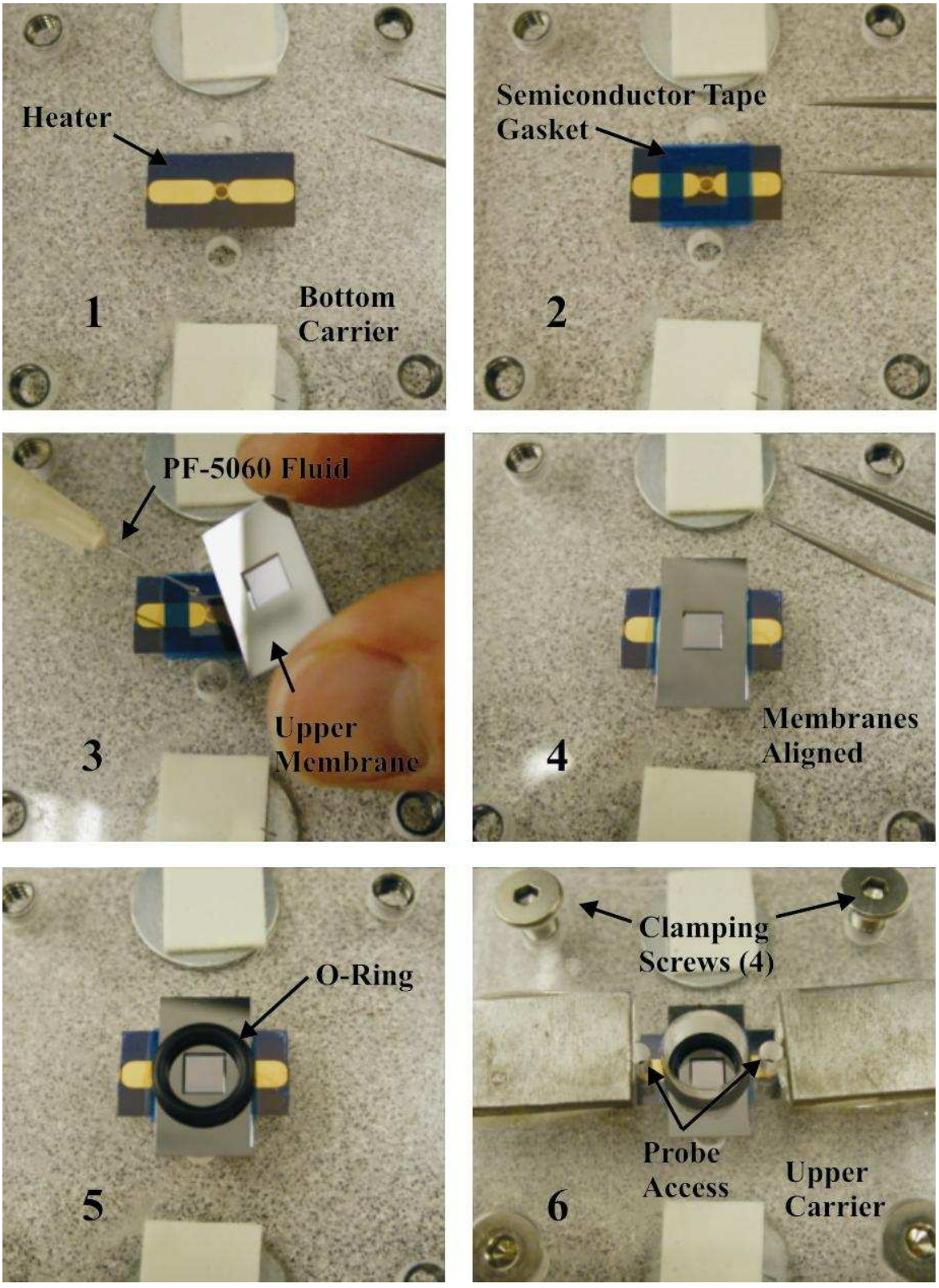

Figure 2.8: Engine assembly procedure.

2.2 EQUIPMENT

Once an engine has been assembled, it is now ready to operate in conjunction with test equipment. The equipment chosen to measure the resonant frequency of the engine provides a means to actuate the membrane generator, measure the initial deflection of the membrane generator, measure the vibration response of the upper membrane to actuation, and finally to collect dynamic measurements for further analysis.

2.2.1 Pulse System

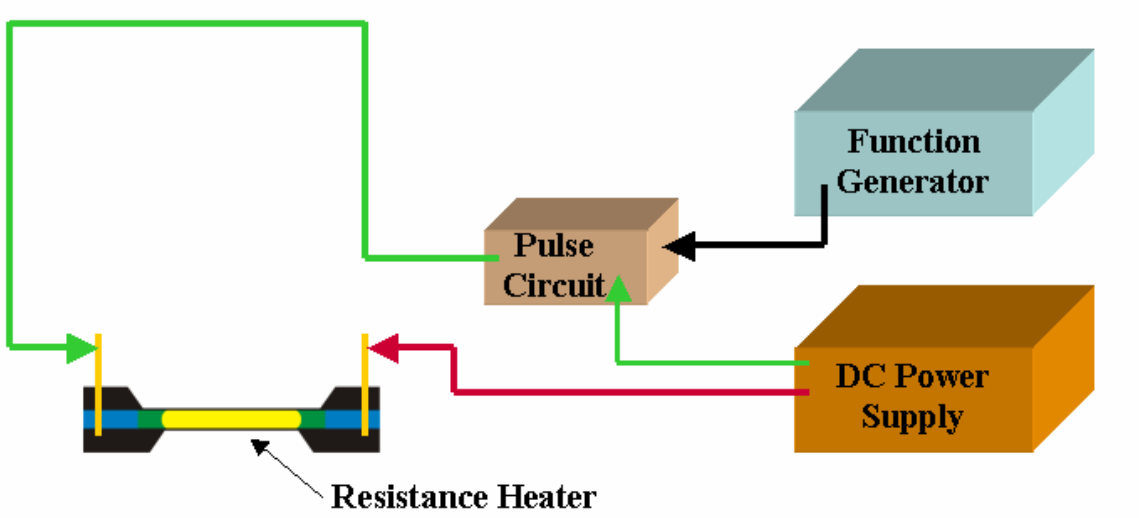

Figure 2.9: Pulse system schematic.

The pulse circuit provides a means to apply and control voltage across the resistance ring heater. A schematic of its components is shown in Figure 2.9. An arbitrary function generator (AFG), Tektronix model AFG-310, allows for precise control of the duration and frequency of heat applied to the engine. A DC power supply, Agilent Model E3610A, provides a means to control the voltage across the resistance heater. Finally a transistor-transistor-logic (TTL) circuit built in-house provides a means to open and close the voltage across the resistance heater based on a trigger input from the AFG.

A circuit diagram for the TTL circuit is shown in Figure 2.10. This system provides large flexibility in how the engine can be actuated. The AFG can output a square wave with any duty cycle, at any frequency, to the TTL circuit, closing the circuit with the power supply, providing voltage across the heater over the range of the power supply. Also, the AFG can be set up to manually trigger, sending a single pulse with a controlled pulse length to the TTL switch, allowing for a heat impulse from the ring heater.

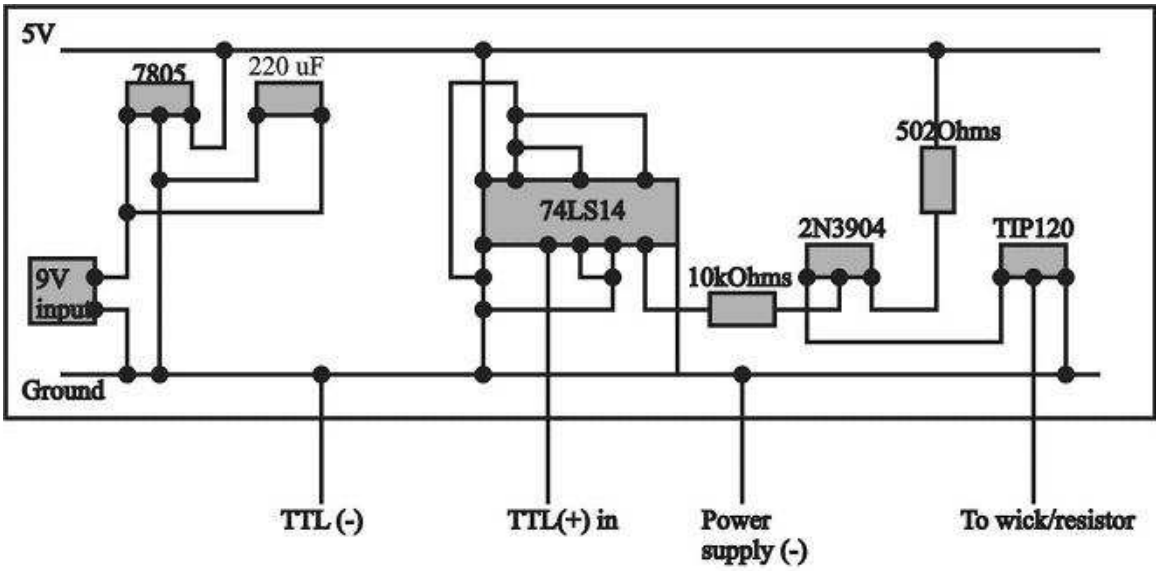

Figure 2.10: TTL Circuit Diagram [69].

2.2.2 Laser Interferometer

The resonant frequency of a membrane is highly dependent on its mean deflection, thus the reason membranes are commonly used to measure differential pressure across their faces [22]. In the same way, the initial deflection of the upper membrane in the engine, after loading, can result in resonant frequency shifts. For this reason it was extremely important to measure the membrane initial deflection. In order to do this, a Michelson interferometer was used. Light from a Nd:YAG laser is run through a beam splitter, where it is directed into two paths. It is reflected off of a reference mirror and the surface of the upper membrane. The reflected light from both paths travels back to the beam splitter where it is recombined. If the surface of the mirror and upper membrane are not the exact same distance from the beam splitter, or if the membrane is deflected, interference patterns are created in the recombined light. The interference patterns, or interferogram, can then be viewed through a long distance microscope. A schematic of the interferometer setup is shown in Figure 2.11. A more detailed discussion of the interferometer operation is included in reference [70]. A typical interferogram for a quarter of a 4 mm upper membrane assembled in an engine is shown in Figure 2.12. Each interference pattern, or fringe, represents 266 nm of out of plane deflection. Interference patterns are easily counted within 2 fringes resulting in a +/- 0.5 μm error.

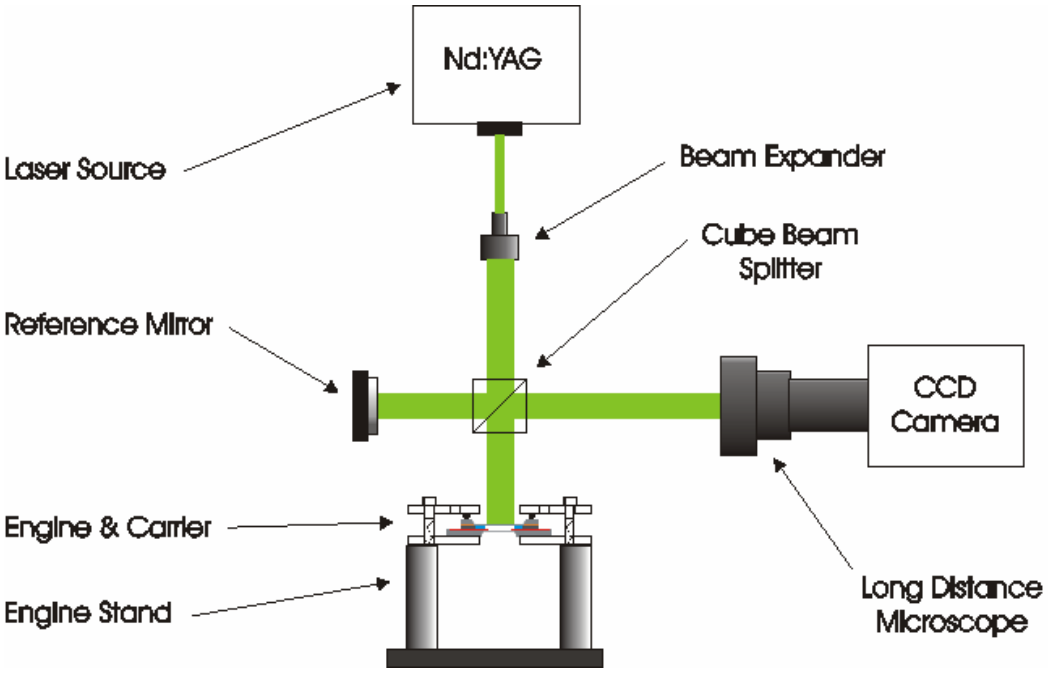

Figure 2.11: Schematic of interferometer with assembled engine.

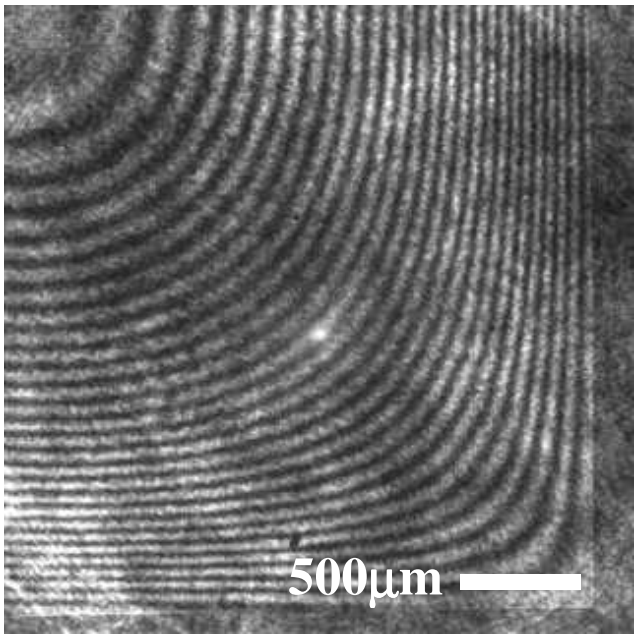

Figure 2.12: Typical interferogram for 4 mm upper membrane assembled in engine.

The interferometer setup also doubles as a microscope that can image the bubble size within the engine. For this to work the laser system is turned off and a cloth is placed over the reference mirror. The engine carrier is then placed upside down, with the heater membrane on top. Front lighting through the beam splitter allows the bubble to be viewed through the transparent heater membrane. If the upper membrane is bare silicon, then the engine can be backlit with a fiber optic light, and the light can pass through the engine. This resulting image of a backlit engine with the bubble and ring heater is shown in Figure 2.13.

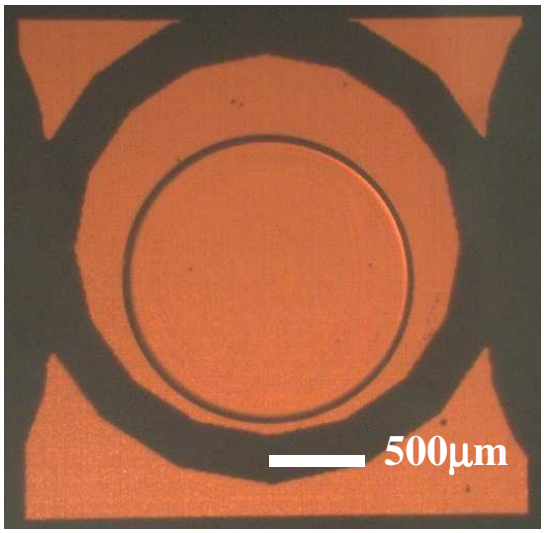

Figure 2.13: Image of bubble and ring heater taken by back lighting interferometer setup.

2.2.3 Laser Vibrometer

The laser vibrometer is used to measure the vibration amplitude of the upper membrane in an engine. The specific vibrometer used was a Polytec OFV-5000 with a VD-06 velocity output decoder. The basic operating principle of the vibrometer is similar to that of an interferometer. The primary difference with this system is that it

uses a frequency modulated helium-neon laser, which is reflected off of a vibrating surface back to a sensor head which measures the change in frequency. The change in frequency of the modulated laser light is due to the Doppler effect. As the membrane deflects towards the source and sensor the modulated light of known frequency reflects off of the membrane, essentially compressed, resulting in a positive frequency shift to the reflected light. Likewise, when the membrane moves away from the sensor it results in an extension or decrease in frequency of the source modulated frequency. This principle is illustrated in Figure 2.14. The change in frequency is then converted to an analog voltage signal that can be measured with various data acquisition equipment, such as an oscilloscope or LabView data acquisition board.

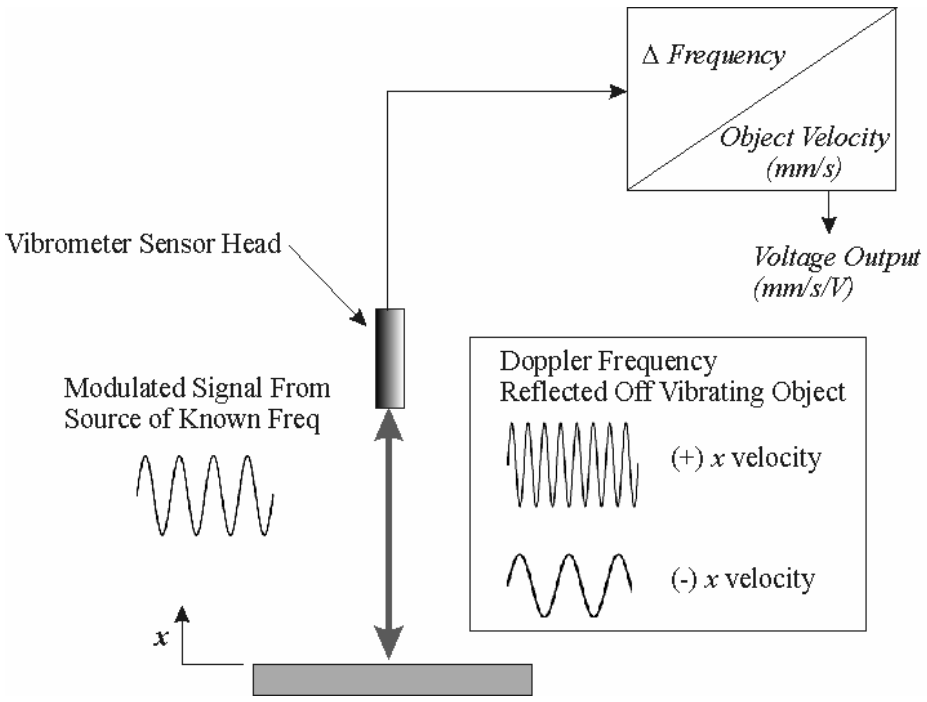

Figure 2.14: Principle of operation of Doppler effect in vibrometer resulting in velocity output.

The vibrometer was configured to measure over the 10 mm/s/V range with the VD-06 velocity decoder. This configuration allowed measurements in the 0 to 350 kHz range with a linearity error < 0.1% and a frequency-dependent amplitude error +/- 0.05 dB for a reference frequency of 1 kHz, as specified by the manufacturer [71]. The time response of the vibrometer output lagged the actual membrane vibration by 12 μs. The VD-06 decoder was also configured for high and low pass filters set at 20 kHz and 0.1 kHz, respectively.

CHAPTER 3

MEASURING RESONANT FREQUENCY

3.1 FORCED VS. FREE VIBRATION

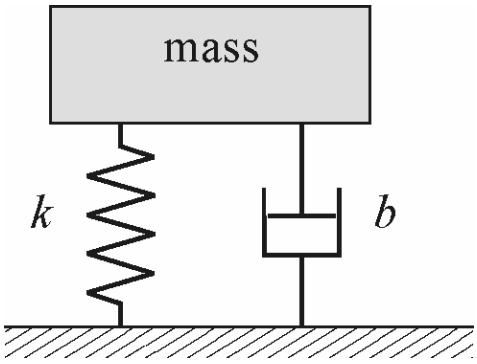

Figure 3.1: Mass-spring-damper system.

The engine is analogous to the one-degree-of-freedom mass-spring-damper system elementary to system dynamics, shown in Figure 3.1 [72]. The first-mode resonant frequency of a mass-spring-damper system can be determined in two ways. The first method involves measuring the frequency response of the mass to an oscillating force. The second method involves measuring the vibration of the mass once it is released from a position away from rest. For convenience the methods will be referred to as the forced vibration method and the free vibration method.

3.1.1 Forced Vibration Method

Forced vibration, by definition, requires a sinusoidal force to physically drive the displacement of the mass. The sinusoidal force can be varied by incrementally sweeping a range of frequencies suspected to encompass the resonant mode. By varying the frequency of the driving force and measuring the amplitude of the vibration, a specific frequency can be determined at which maximum displacement amplitude occurs. At this

point the phase angle between the driving force and the displacement will shift to 90º. The driving frequency resulting in the maximum vibration amplitude and a 90º phase lag defines the first resonant mode of the system. Figures 3.2 (a) and (b) show the forced mass-spring-damper system and its hypothetical response to a range of frequencies above and below the resonant frequency.

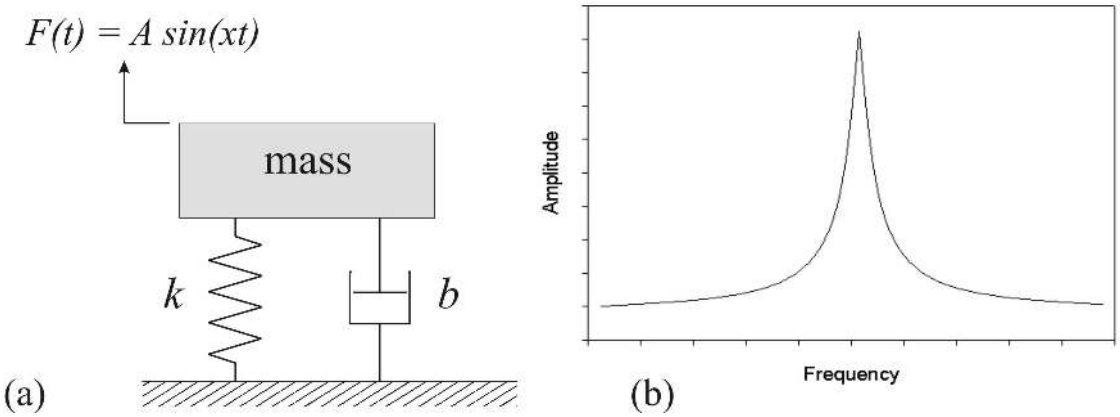

Figure 3.2: (a) Forced vibration mass-spring-damper system and (b) frequency response.

In regards to the engine, it may be possible to provide forced vibration in one of three ways. First, the generator membrane is designed for actuation with thermal energy provided by the ring heater. However, the engine is limited to operate at rates at which adequate heat transfer into and out of the engine can occur. As discussed in Chapter 1, driving the engine at a large range of frequencies is not possible, as the system cannot reject pulsed heat fast enough without active cooling. Forced vibration by thermal actuation is therefore ruled out as a method to determine the resonant frequency. An alternative approach is to drive the engine to its resonant frequency by an external force. An example might be a speaker in close proximity to the engine. The speaker could then be driven to vibrate over a range of frequencies which would result in pressure waves

being transferred through the air and acting on the engine. However, the speaker would need to have a wide band-gap operating at constant amplitude. Initial tests with a decibel meter showed that it would be difficult to achieve constant amplitude from a speaker, as the sound pressure varied significantly over the frequency ranges of interest. As a final consideration to forced vibration, since the piezoelectric effect is reversible, the membrane generator itself can serve as a means to actuate its own vibration, by applying an AC voltage across its electrodes. Measuring the membrane vibration amplitude to the driving voltage will then allow an effective means of determining the position of the resonant frequency.

3.1.2 Free Vibration Method

Free vibration involves displacing the mass of a system some distance away from rest and then releasing it to observe its response. This response can also be observed by displacement produced from an impact force on the mass. In this case, the response is often referred to as an "after-ringing" effect. If slight damping is present, the free vibration amplitude of the mass decays exponentially. Figure 3.3 shows the response of a mass-spring-damper system to an impact force. The oscillation frequency of the mass about its rest position is the first resonant mode of the system.

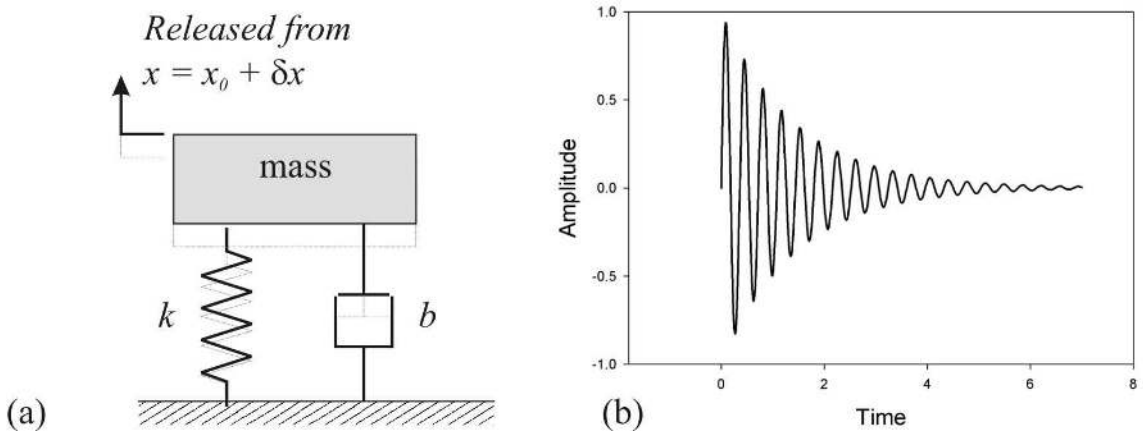

Figure 3.3: Free vibration response to an impact force.

The free vibration of the engine can also be used to provide resonant frequency information. This can be done by applying an impact to the upper membrane and observing its deflection response. The easiest way to provide a controlled impact to the engine is by applying a very short heat pulse through the ring heater. A single heat pulse will cause a pressure pulse in the cavity as vapor is created and condensed rapidly. The "after-ringing" response of the upper membrane can then be analyzed to provide the first resonant mode of engine vibration.

3.1.3 Pursuing an Experimental Method

The forced vibration and free vibration methods of determining system resonant frequency each have their advantages. The forced vibration method provides information about the vibrating characteristics of the engine over a broad range of operating frequencies both near the resonant frequency and far away from it. The method also allows for good precision in determining the resonant frequency, because the precision is largely limited by the size of the incremental frequency change. Near the resonant frequency, very small increments will result in a very precise position of the resonant

mode. Alternatively, the free-vibration method applies a thermal pulse to the working fluid resulting in a pressure spike within the engine cavity. Using heat to actuate the upper membrane is akin to the final desired operation of the engine, where heat is transferred into and out of the engine. The free-vibration experiment is also very quick, as only one "after-ringing" response must be measured to determine the resonant frequency. Due to the advantages of each method, both methods were developed for application to the P3 micro engine.

3.2 FORCED VIBRATION EXPERIMENT

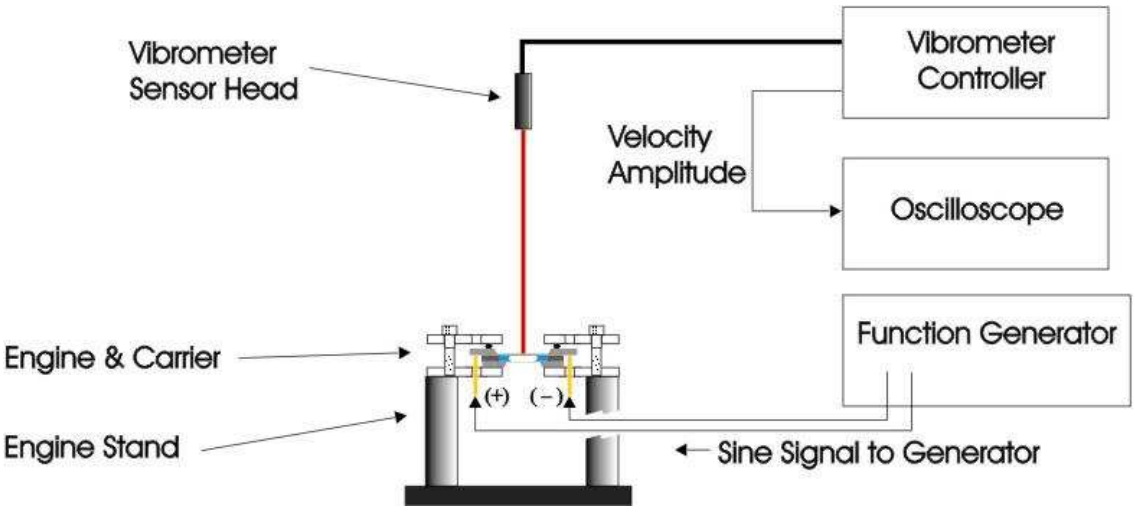

Figure 3.4: Forced vibration experimental schematic.

The forced vibration experiment involved exciting vibration of the generator membrane through a function generator, and then measuring the vibration amplitude with a laser vibrometer. A schematic of the experimental setup for forced-vibration is shown in Figure 3.2.1. An engine was assembled with a standard 3 mm generator membrane,

150 μm cavity thickness, a 500 mm bubble, and 5 μm initial static deflection. The initial static deflection defines the out of plane deflection of the upper membrane after assembly. The assembled engine was then placed on the vibrometer measuring stand where the laser was aligned with the center of the generator membrane. Probes were then attached to the carrier to contact the generator electrodes. A function generator was connected to the probes with the positive terminal contacting the gold upper electrode and the negative connected through a probe to the platinum bottom electrode. A sine function with 5V amplitude was applied to the generator, and the peak-to-peak velocity of the membrane was measured with the vibrometer connected to an oscilloscope. The velocity amplitude was monitored while the frequency of the driving force was varied from 2 kHz to 16 kHz in 0.1 kHz increments. Maximum amplitude was measured at around 10.1 kHz, specifying the resonant frequency. The experimental results are shown in Figure 3.4. These results show that the first resonant mode of an assembled engine can be found by forced vibration provided by the generator membrane.

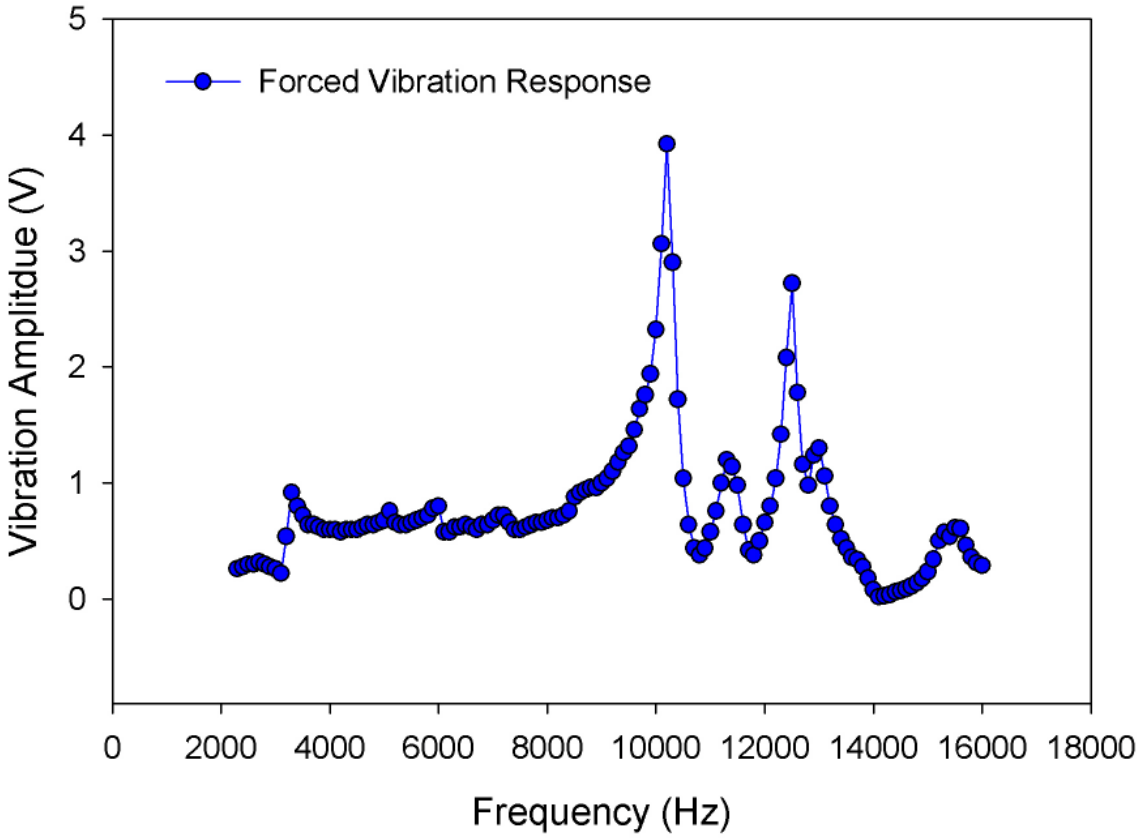

Figure 3.5: Frequency response of the forced vibration of a 3 mm generator membrane loaded in an engine with a 150 μm cavity depth, 500 μm bubble diameter, and 5 μm initial static deflection.

3.3 FREE VIBRATION EXPERIMENT

The free vibration response of the same engine assembly measured in the forced vibration experiment to a heat pulse was measured using the vibrometer. The vibrometer laser was aligned and focused at the center of the 3 mm generator membrane loaded in an engine. An oscilloscope was used to monitor the vibrometer velocity output. The velocity decoder was set to measure velocity in the range of 10 mm/s/V. A single pulse was then sent to the heater by a manual trigger of the pulse circuit. Through experimentally successful measurements of an "after-ringing" effect, a standard voltage

amplitude of 3 V with a 200 μs pulse length was chosen for free vibration tests. A schematic for the experimental setup for free vibration of a membrane generator is shown in Figure 3.6. The free vibration of the 3 mm generator assembled in an engine with a 150 μm cavity depth, 500 μm bubble diameter, and 5 μm initial deflection is shown in Figure 3.7. For comparison the free vibration response of a 3 mm silicon membrane assembled in an engine with the same configuration is shown in Figure 3.8. A beating frequency can be observed within the "after-ringing" response of the 3 mm generator engine, possibly signifying that the resonant frequency of the generator membrane is near that of the lower 2 mm heater membrane. However, the beating effect is not apparent in the "after ringing" response of the 3 mm Si membrane engine, signifying that the resonant frequency of the Si membrane is not near that of the lower 2 mm heater membrane. This is best shown by considering resonant frequencies of the 3 mm generator, 3 mm Si membrane, and 2 mm heater membrane independently. The resonant frequency of the 3 mm generator has been found to be about 25.7 kHz in vacuum [73]. The theoretical resonant frequencies of the 3 mm Si membrane and 2 mm heater membrane in a vacuum can be approximated theoretically from [74] as:

$$f_{11} = \frac{1}{2}\sqrt{\frac{2 \cdot \sigma_0}{\rho \cdot L^2}} \qquad 3.1$$

with: f_{11}: first resonant mode of vibration

σ_0: residual stress, 30 MPa

ρ: membrane material density, 2300 kg/m^3

L: membrane side length

The expected resonant frequencies of each membrane in a vacuum are shown in Table 3.1. Since the resonant frequencies of the 3 mm generator and 2 mm heater membrane in vacuum are close, it is likely that when they are coupled in the engine system a beating frequency will occur. A beating effect will be less apparent at with the 3 mm Si membrane because its resonant frequency is far away from that of the 2 mm heater membrane.

Membrane	**Resonant Frequency (kHz)**
3 mm Generator [73]	25.7
3 mm Si Membrane	19.0
2 mm Heater Membrane	28.5

Table 3.1: Theoretical resonant frequencies of 3 mm generator, 3 mm Si membrane, and 2 mm heater membrane in a vacuum.

The beating frequency makes it difficult to determine the resonant frequency directly therefore a Fourier transform must be used. Performing a Fast Fourier Transform (FFT) of the "after-ringing" response converts from the time domain to the frequency domain, providing frequency response information. The free-vibration experiment can then be compared to the forced vibration experiment for both the engine assembled with a generator and a membrane. The FFTs of the 3 mm generator and Si membrane engines were performed using the built in Fourier analysis subroutine within Excel. The FFTs were conducted following the method outlined in reference [75]. One problem associated with taking an FFT of the "after-ringing" response is the resolution of the transform. The resolution of the Fourier transform is given by the sampling frequency divided by the

total number of samples. The total number of samples must be equivalent to 2^n, where n is a positive integer. For the 3 mm generator engine, the oscilloscope provided time resolution at 1 x 10^{-6} seconds, or a sampling frequency of 1 MHz. Because the sampling period was only 2.5 x 10^{-3} seconds, providing 2048 data points, the Fourier transform resolution is only 488 Hz. In contrast, the response of the 3mm Si membrane engine was measured over a longer duration resulting in a frequency resolution of 122 Hz. Comparing the FFTs of the "after-ringing" responses to the forced vibration response in Figure 3.9 shows that the same resonant peaks can be observed for the 3 mm generator engine. However, the FFT does not provide adequate resolution for locating the peak amplitude due to the small time duration considered. The resonant frequency of the 3 mm Si membrane engine is much less at around 2.5 kHz.

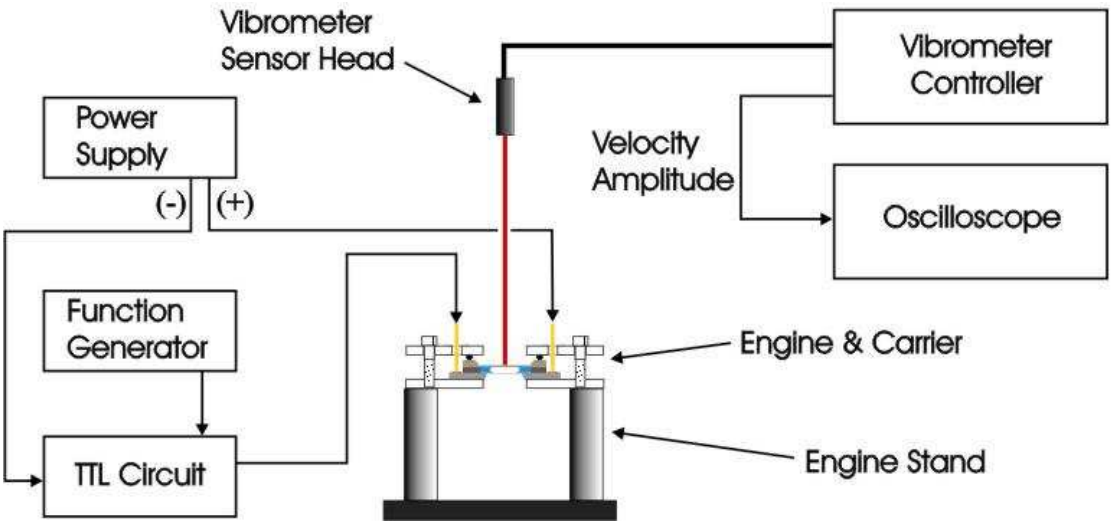

Figure 3.6: Schematic of free vibration experimental setup.

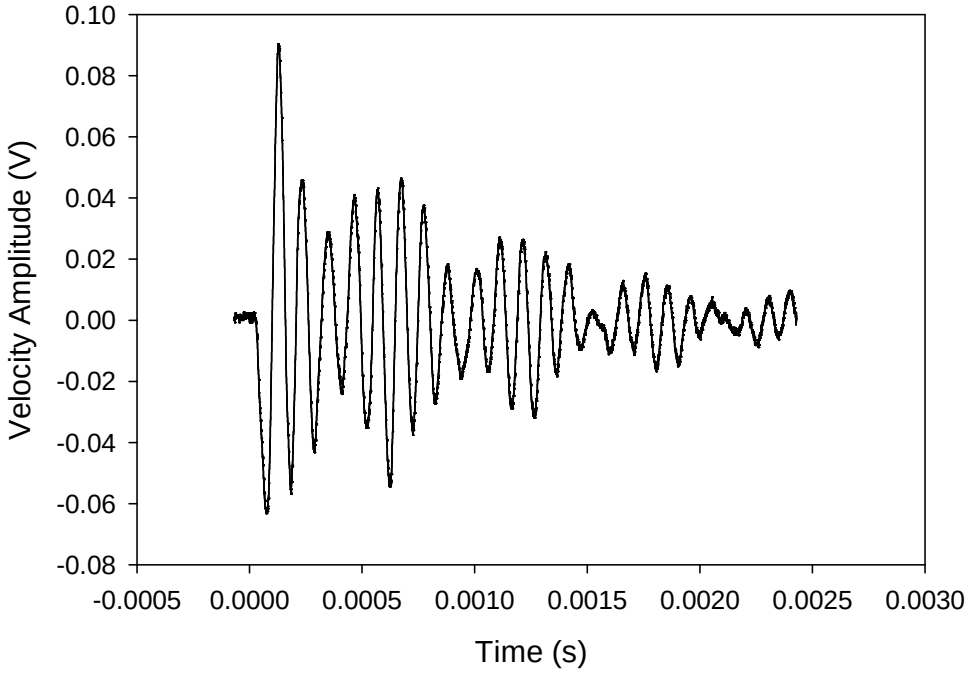

Figure 3.7: Free vibration "after-ringing" of engine with 3 mm generator, 150 μm cavity depth, 500 μm bubble diameter, and 5 μm initial static deflection.

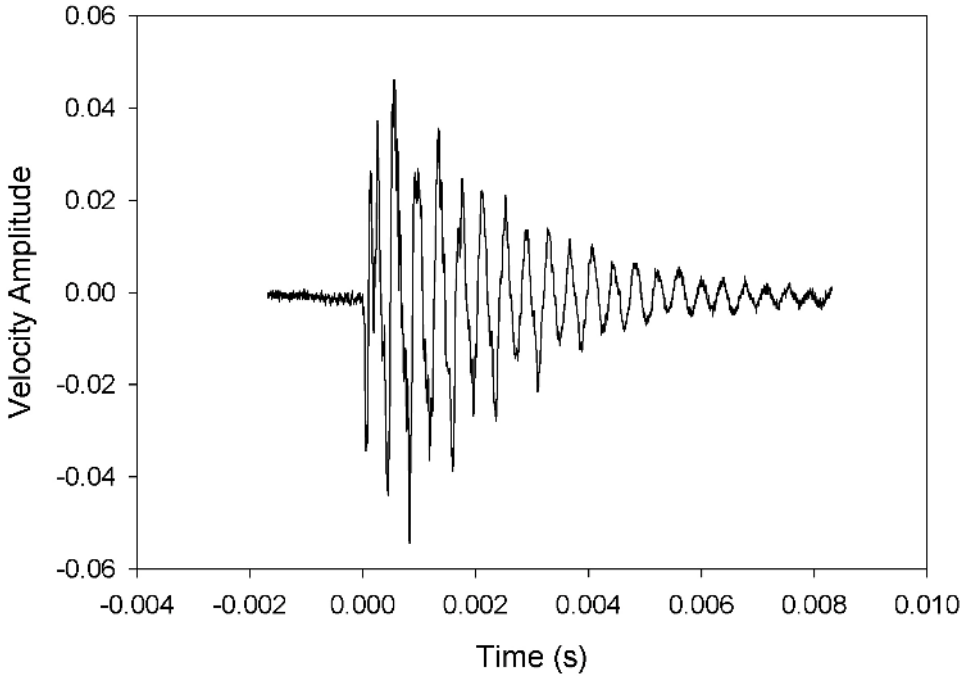

Figure 3.8: Free vibration "after-ringing" of engine with 3 mm Si Membrane, 150 μm cavity depth, 500 mm bubble diameter, and 5 mm initial static deflection.

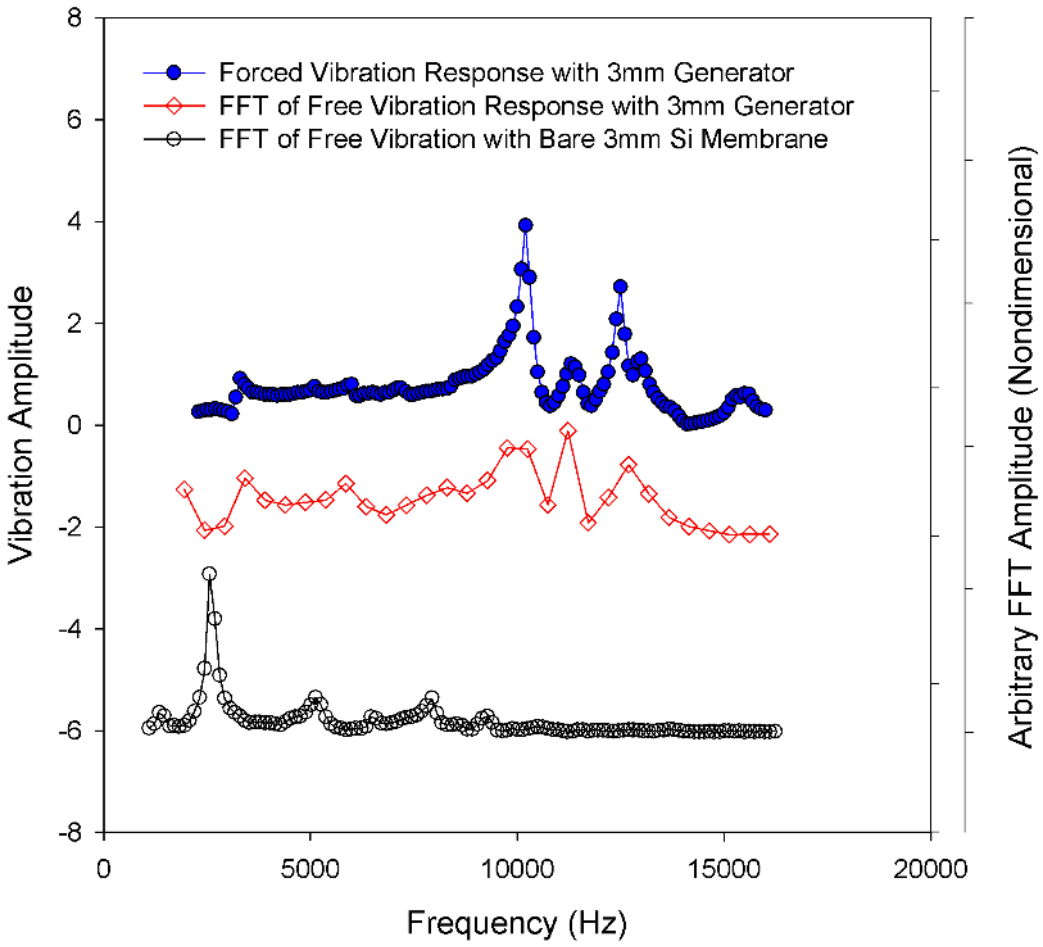

Figure 3.9: Comparison between forced vibration of engine with 3 mm generator and free vibration of engines assembled with 3 mm generator and 3 mm Si membrane.

In order to make an additional attempt of the free vibration experiment with out large effects from beating frequencies, the generator membrane was replaced with a 4 mm bare silicon membrane. This was done to further reduce the upper membrane resonant frequency to a point at which the beating frequency would not occur. Using a bare membrane has the added advantages of easier optical access, less fabrication processes, and a lower residual stress.

A free vibration experiment was performed on an engine assembled with a 4 mm, 2.2 μm thick bare silicon membrane, 150 mm cavity depth, and 1170 mm bubble diameter. The free vibration response to the heat pulse is shown in Figure 3.10 with the beating frequency successfully eliminated. Once the velocity "after-ringing" was available, the time and amplitude data were imported to an Excel spreadsheet. The data was cropped to remove the initial zero velocity condition. The cut off position is shown as the dashed line in Figure 3.10. The cropped data was then exported into a SigmaPlot spreadsheet, where it was plotted with a two-dimensional scatter plot, with time on the x-axis and voltage amplitude from the vibrometer on the y-axis. A curve fit was then performed through a SigmaPlot curve-fit utility for a 4-parameter damped sinusoid. The equation for the generated curve, of the form:

$$y = a \cdot e^{-\frac{x}{d}} \sin\left(\frac{2\pi x}{b} + c\right) \qquad 3.2$$

provided resonant frequency information for the free vibration engine, defined in Hz as the inverse of the coefficient b. Figure 3.11 shows a curve-fit and equation for the "after-ringing" response shown earlier in Figure 3.10.

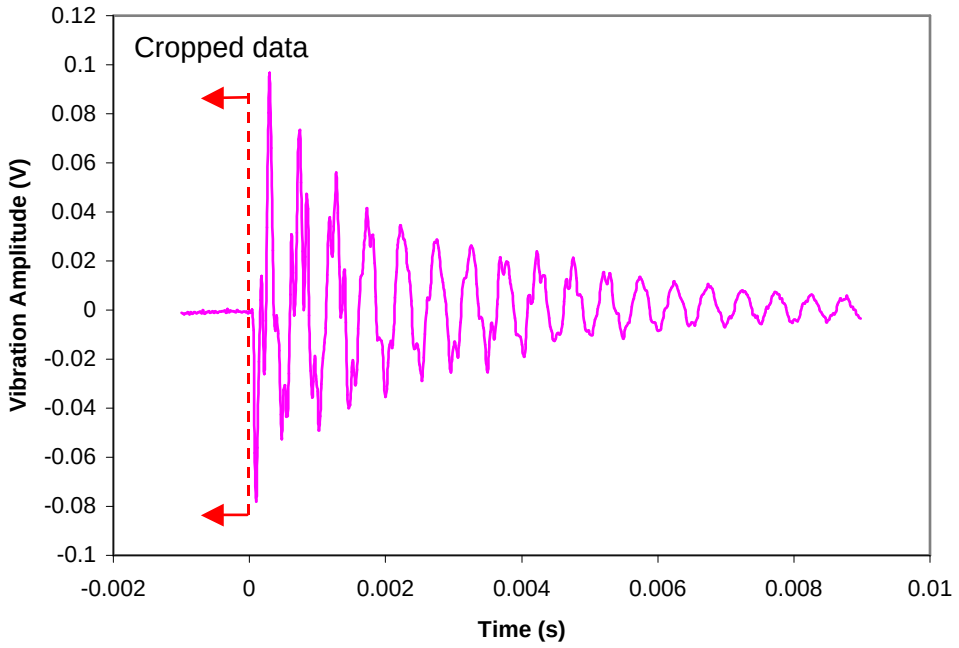

Figure 3.10: Typical Velocity Response of an Engine to Heat Pulse Showing "After-Ringing" Effect

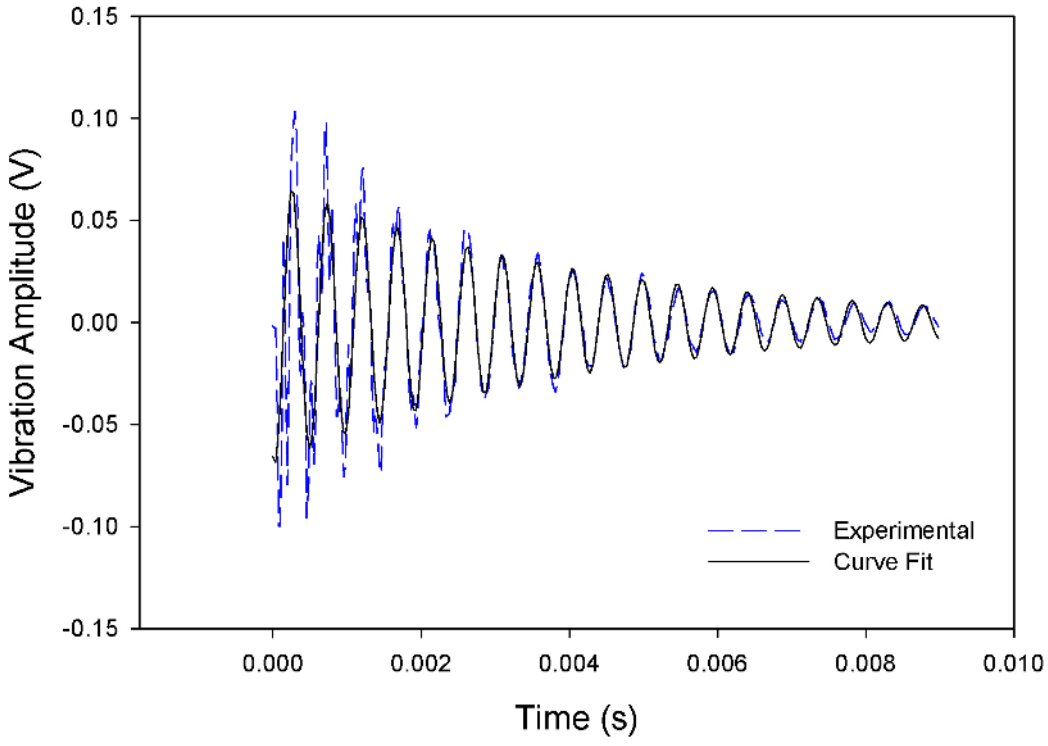

Figure 3.11: Curve-Fit of Free Vibration of Engine.

In order to test the repeatability of the free vibration test, a single assembled engine was tested ten times. The engine configuration was a 2.2 μm thick silicon upper membrane with a 4 mm side length. The cavity thickness was set at 150 μm by using two layers of semiconductor tape. The bubble size was measured after the measurement set at 1170 μm. The lower membrane consisted of a 2 mm membrane with a 1.8 mm ring heater. A single pulse with amplitude of 3 V and duration of 200 μs was applied across the 1.4Ω resistance heater with the pulse circuit. The "after-ringing" response was measured with the laser vibrometer for ten manual triggers over 210 seconds. The resonant frequency was then extracted from a SigmaPlot curve fit for a damped-sinusoidal. The mean of resonant frequencies measured was 2037 Hz. A *Student t* distribution for a 95% confidence interval put the repeatability of the free vibration measurement of the resonant frequency at ± 8.6%. Figure 3.12 shows the variance observed in 10 free vibration tests of a single engine.

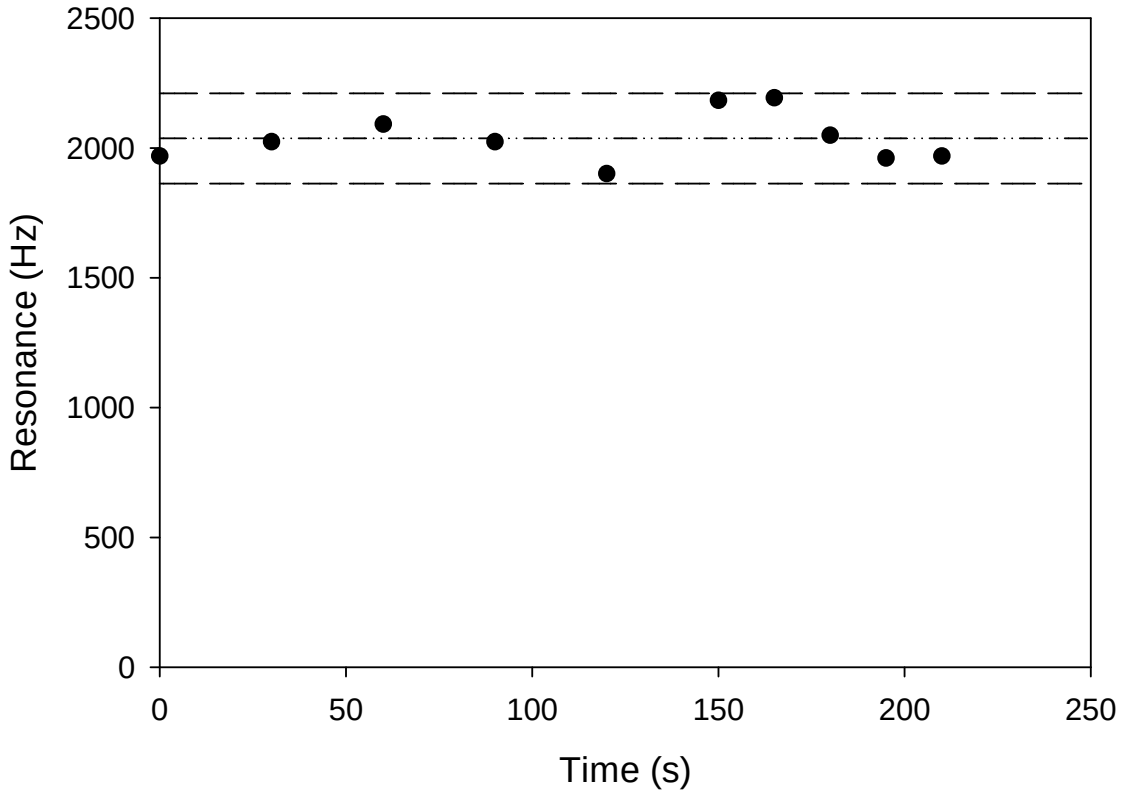

Figure 3.12: Repeatability of engine resonant frequency measured by free vibration method.

CHAPTER 4

ENGINE PARAMETRIC STUDY

4.1 ENGINE PARAMETERS

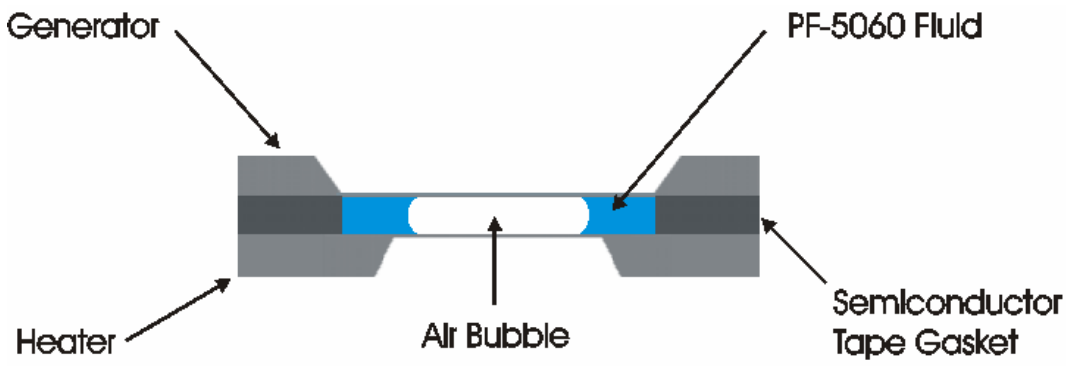

Figure 4.1: Schematic of engine [76].

The goal of the parametric study of engine resonant frequency was to determine experimentally how individual engine components affect the resonant operation of a single engine. Engine parameters can then be used to tailor the operating frequency of an engine to specific requirements, possibly determined by limited heat rejection rates, power requirements, or geometry constraints.

Engine parameters chosen for this study were determined largely from the components of the engine that were readily adjustable, and then from literature showing which components would most likely influence the resonant frequency. In its basic form, the engine consists of a membrane, a two-phase fluid filled cavity, and a heater membrane, shown in Figure 4.1. It was readily apparent that the parameters providing the greatest adjustability were the membrane size, the liquid/vapor ratio of the working fluid, and finally, the cavity thickness. The literature also showed that each individual

parameter could have an influence on the resonant frequency of similar membrane [40], membrane-fluid coupled [48], and membrane-fluid-cavity coupled [35,58,67] systems.

For each stage of this study a 2.2 μm thick bare silicon membrane was used in place of the membrane generator. The bare silicon membrane provided optical access to measure the diameter of the liquid-vapor interface. Also, since the cross-section of the membrane generator is not uniform, as shown in Figure 4.2, the bare membrane provided a means to change the membrane size without performing a rigorous analysis to determine the appropriate coverage area. Another advantage to using the bare membrane was that it required fewer processing steps and resulted in decreased fabrication turn-around time, cost, processing inconsistencies, and lower residual stress.

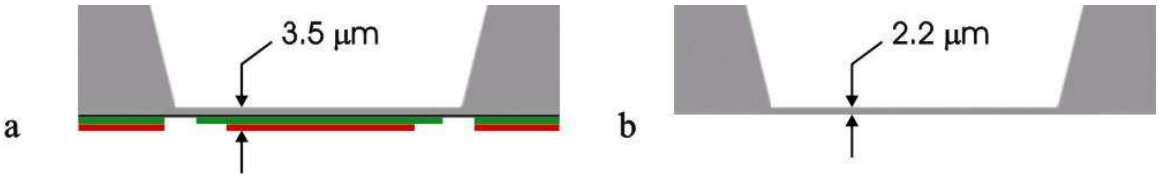

Figure 4.2: (a) Generator cross-section and (b) Silicon membrane cross-section.

4.2 EXPERIMENTAL PROCEDURE

The experimental procedure for measuring the resonant frequency of any engine configuration is basically the same, independent of test parameters. The free vibration method developed in Chapter 2 was used for all configurations. The only differences between varying engine configurations were the components used in assembly. For clarity, a schematic of the free vibration experiment is shown in Figure 4.3. Once an engine was assembled in its carrier, it was placed on a stand, centered under the laser vibrometer sensor head. Probes were then placed in contact with the heater electrodes

and connected to the pulse circuit. The vibrometer laser shutter was then opened and a check was performed to ensure the laser was centered on the membrane, and a maximum signal read by the vibrometer controller was displayed. Next, the pulse circuit was manually triggered by the AFG to provide a 3 V, 200 μs heat pulse across the resistance ring heater. At the same time, an oscilloscope was triggered by the AFG signal to begin recording the velocity output from the laser vibrometer. The oscilloscope trigger was set on "normal" mode to record and save a single "after-ringing" response. Finally, the upper membrane static deflection and engine bubble size were measured using the interferometer equipment.

Following the experiment, the response data and deflection and bubble size were imported into an Excel Spreadsheet. Data analysis was performed using a curve-fit in SigmaPlot to arrive at the resonant frequency of the specific engine configuration.

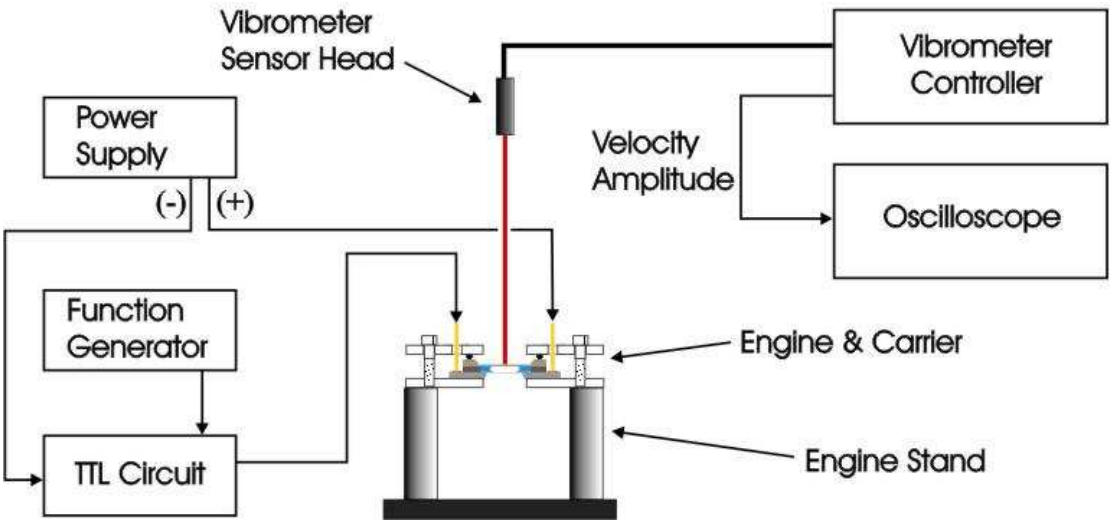

Figure 4.3: Free vibration experiment schematic.

4.3 MEMBRANE GEOMETRY

It was hypothesized that membrane size would have a large effect on the resonant frequency of the engine. The first resonant mode for a square membrane in a vacuum vibrating in the linear regime is given by reference [74] as:

$$f_{11} = \frac{1}{2}\sqrt{\frac{2 \cdot \sigma_0}{\rho \cdot L^2}} \qquad 4.1$$

with: f_{11}: first resonant mode of vibration

σ_0: residual stress

ρ : membrane material density

L: membrane side length

Since the side length contributes to the denominator, an increase in side length will result in a decrease in resonant frequency. The same effect should be observed in engine assemblies.

4.3.1 Membrane Size Experiment

The experiment consisted of testing engines assembled with upper membrane side lengths of 3 mm, 4 mm, 6 mm, and 8 mm. Additional oxide masks to define membrane size were designed and are shown in Figure 4.4 and Figure 4.5. Figure 4.6 shows the relative sizes of the fabricated membranes. The actual membrane sizes were 3.09 mm, 4.10 mm, 6.10 mm, and 8.10 mm, as measured upon completion of fabrication. The engine cavity thickness was held constant at 150 μm. The cavity planar dimensions were scaled with the membrane sizes as shown in Figure 4.7. The difficulty in reproducing exact bubble diameters, which defined the fluid/vapor ratio, required multiple engines to

be assembled and tested for each membrane side length. Ten engines were tested at the 3 mm membrane size, and twenty engines were tested at the 4 mm membrane size. Membranes larger than 4 mm were difficult to seal using the acrylic carrier and semiconductor tape gasket. Although a large amount of effort was put into alternative methods of sealing, a solution could not be found in time to produce a large sample size of larger engines for this study. If fact, only six resonant frequency measurements were made for a 6 mm engine and only two for an 8 mm engine. However, these measurements will be included in the final results, as there is reasonable confidence that their measured resonant frequencies will, at the least, qualitatively show the influence of larger upper membrane size on the resonant frequency of the engine.

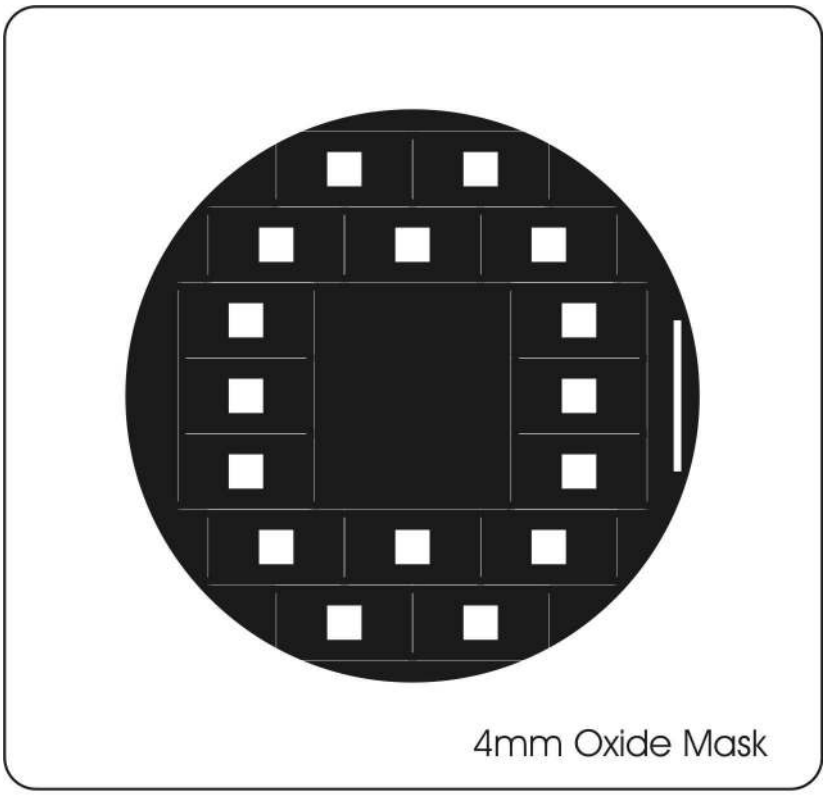

Figure 4.4: Oxide masks for 4 mm silicon membranes.

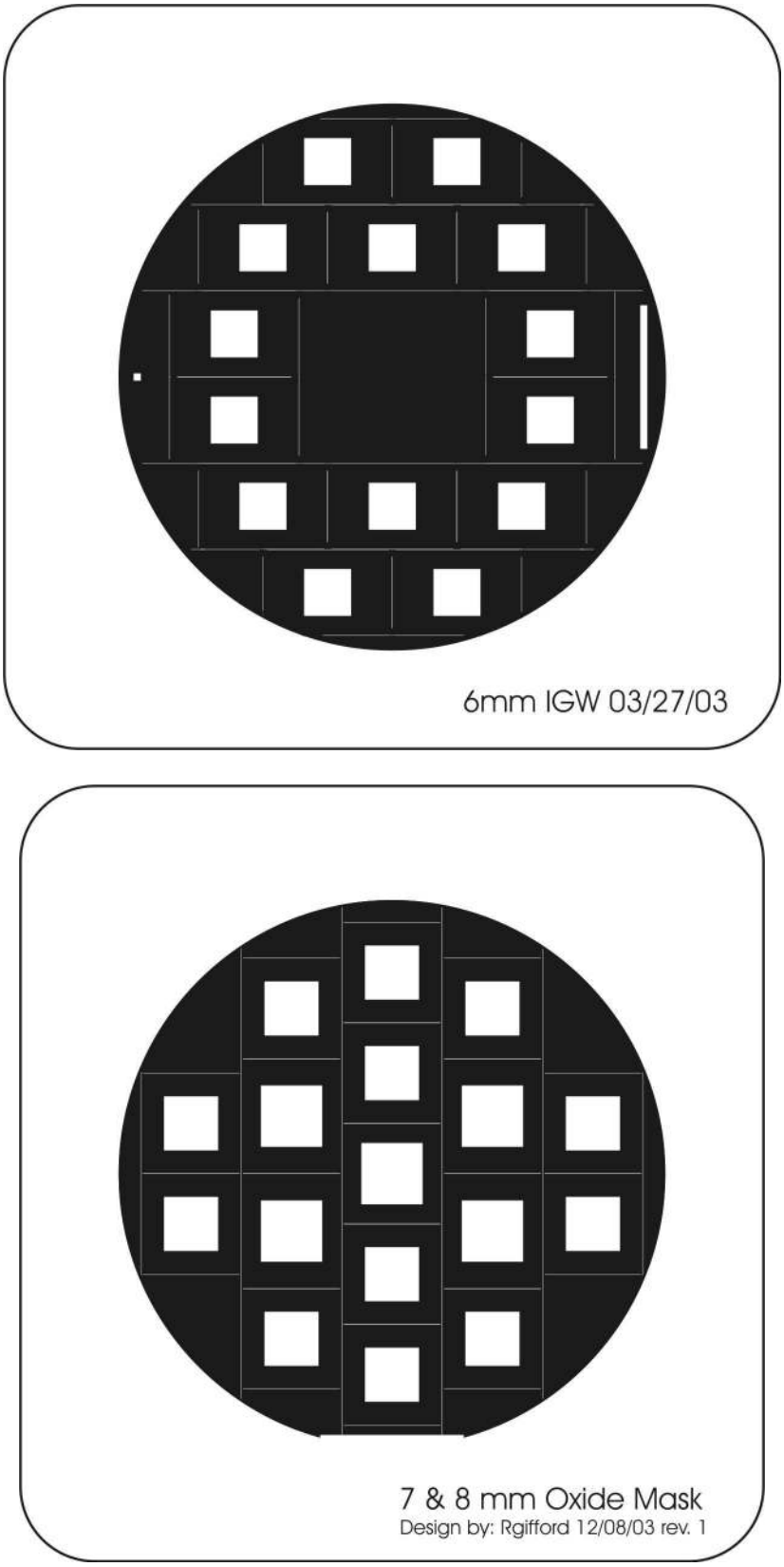

Figure 4.5: Oxide masks for 6 mm and 7 and 8 mm silicon membranes.

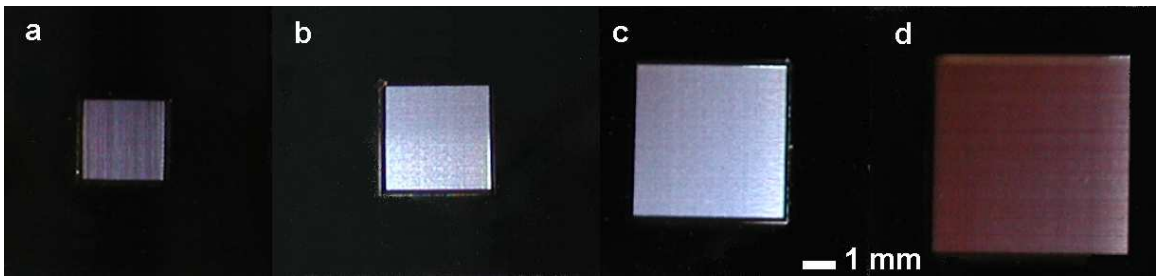

Figure 4.6: Relative sizes of (a) 3 mm (b) 4 mm (c) 6 mm and (d) 8 mm silicon membranes.

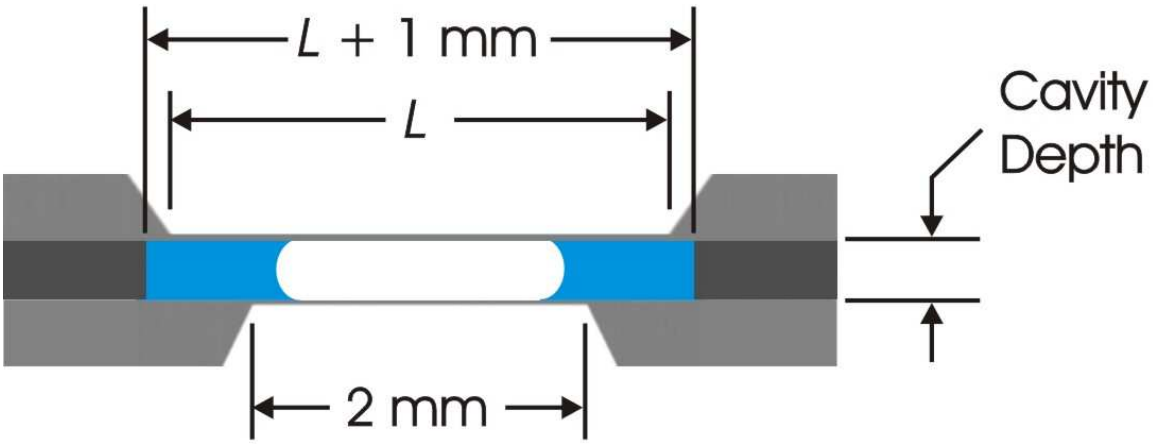

Figure 4.7: Semiconductor tape gasket defining the engine cavity scaled with the membrane side length.

4.3.2 Membrane Size Results

The results of a change in membrane side length are shown in Figure 4.8. As hypothesized, the plot shows an exponential decrease in resonant frequency with an increase in membrane side length. The error bars correspond to a 95% confidence interval of all engines tested, determined for a small sample size Student-t statistical

analysis [77]. The error within each data point is most likely a result of varying membrane deflections and bubble diameters. No error bars are displayed for the 8 mm membrane side length as only two engines were tested, each with a resonant frequency of 416 Hz.

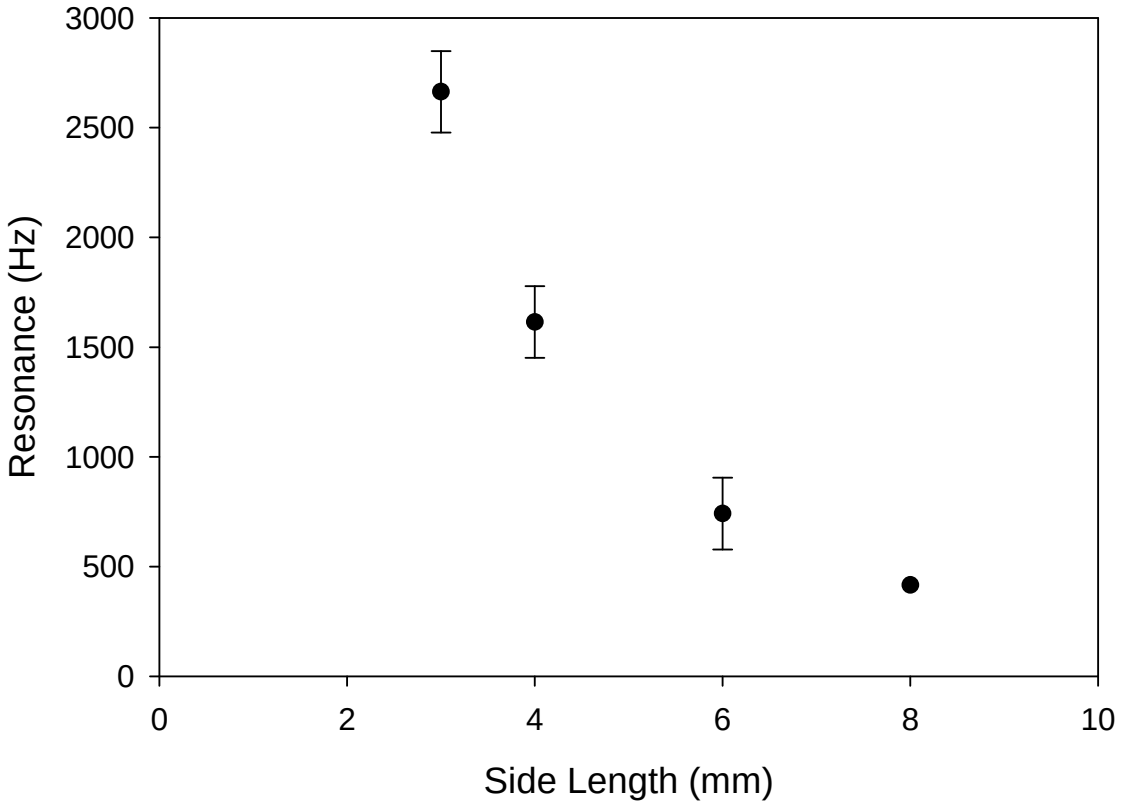

Figure 4.8: Engine resonant frequency as a function of membrane side length.

4.4 BUBBLE DIAMETER

The effect of the fluid/vapor ratio was determined by establishing the bubble diameter of the engine as the parameter of interest. It has been shown in references [48] and [49] that the resonant frequency of a structure in fluid decreases as the fluid density increases, due to added inertia. Therefore, as the bubble size decreases, the fluid in

contact with the membrane would increase, causing an increase in the effective density of the fluid in contact with the membrane. This would result in an expected decrease in engine resonant frequency as the bubble diameter decreases.

4.4.1 Bubble Size Experiment

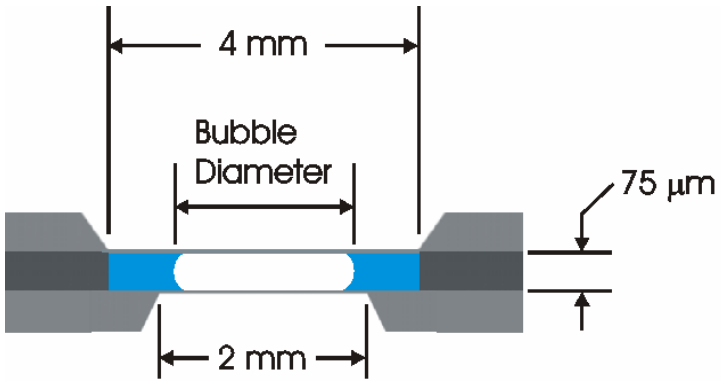

Figure 4.9: Bubble diameter parameter.

Twenty engines were tested with varying bubble diameter based on assembly. Membrane size and cavity thickness were held constant at 4 mm and 75 µm, respectively. A schematic of the test engine is shown in Figure 4.9. Figure 4.10 shows three different bubble diameters assembled in engines. The engines were assembled, and then the resonant frequency was determined using the standard free-vibration test. Bubble size and membrane deflection were measured within one minute of testing.

The bubble diameter was measured using *Scion Image for Windows* release Beta 4.0.2. The outside diameter of the ring heater of 1820 µm was used as a reference scale to determine the actual bubble size. The number of pixels across the diameter of the outside tip of the bubble meniscus was measured within +/- 10 pixels. This corresponds

to an error of +/- 20 μm, based on an average scale value of 2 μm per pixel. Bubble sizes based on assembly varied from 475 ± 20 μm to 1800 ± 20 μm. The average engine deflection was 6 μm with a standard deviation of 2 μm.

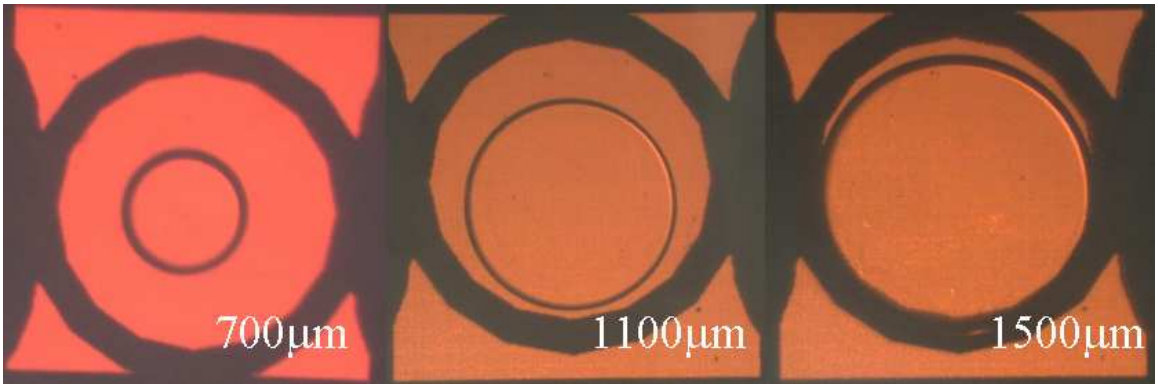

Figure 4.10: Large, medium, and small bubbles assembled in engines with bubble diameters shown.

4.4.2 Bubble Size Results

Resonant frequency was shown to decrease as the bubble diameter decreased. Figure 4.11 shows the resonant frequency of multiple assemblies of 4 mm engines with 75 μm cavity depth and varying bubble diameters. The error bars specify the repeatability of the free-vibration test as specified in Chapter 2. A 95% confidence interval was also determined for the experiment by performing a prediction interval statistical analysis within SigmaPlot. The prediction interval specifies the 95% confidence interval for the population. The maximum and minimum bubble diameters resulted in resonant frequencies of 1110 Hz and 1330 Hz, respectively. This results in only an 8.2 % change in resonant frequency with a 75% increase in bubble diameter. The

repeatability of the free vibration test used was shown to be +/- 8.6 %. This allows question to the reliability of controlling resonant frequency with bubble diameter. This result supports the hypothesis that added mass effects occur due to the liquid in contact with the membrane.

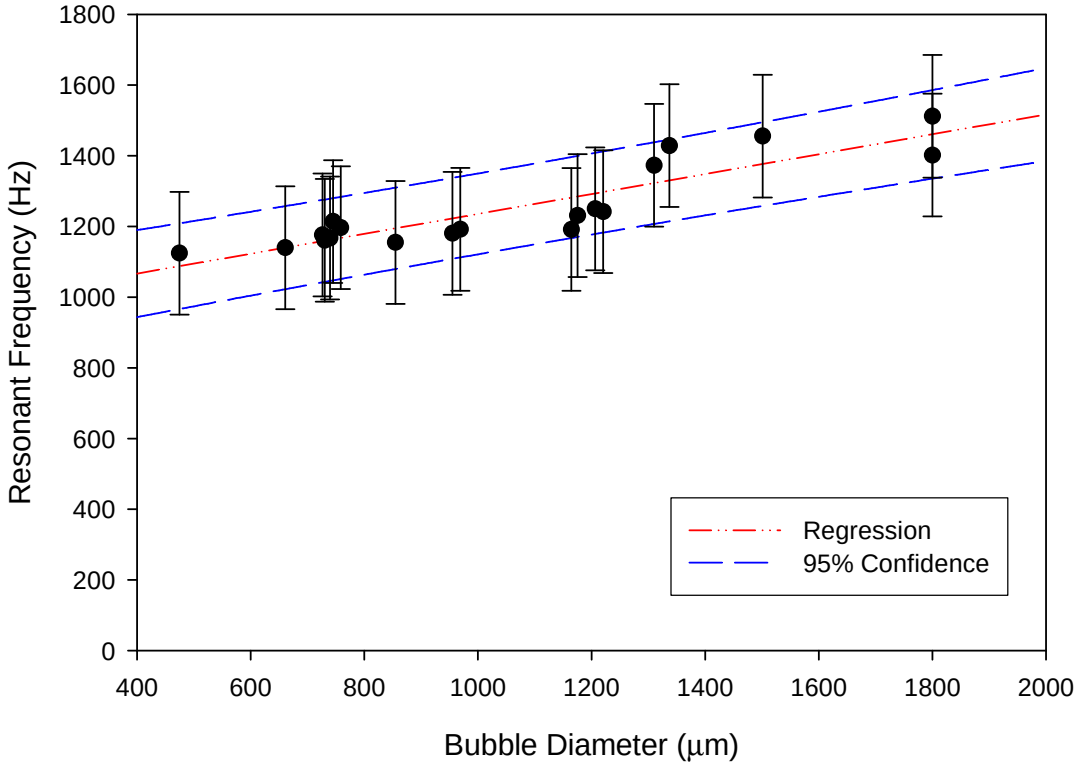

Figure 4.11: Resonant frequency of a 4 mm engines with 75 um cavity depth at varying bubble diameters.

4.5 CAVITY DEPTH

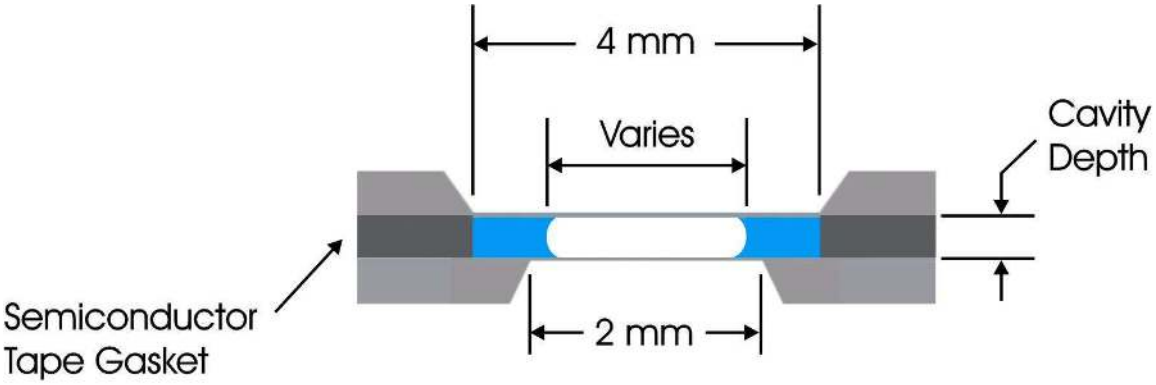

Figure 4.12: Engine cavity depth parameter.

The third and final parameter that was of interest was the effect of engine cavity depth on resonant frequency, shown in Figure 4.12. The literature also showed that structures vibrating in a non-compressible fluid near a solid wall exhibited an increase in effective mass as the distance between the structure and the solid wall decreased [58,67]. This phenomena leads to the hypothesis that a change in cavity depth will result in a shift in resonant frequency, due to a shift in the effective mass of the engine. Specifically, a decrease in cavity depth should result in an increase in the effective mass and a decrease in resonant frequency.

4.5.1 Experimental Methods

Measuring the free vibration response of engines with various cavity depths while keeping the membrane size constant allowed the effect of cavity depth on resonant frequency to be observed. The upper and lower membranes in this experiment consisted of a 4 mm bare silicon upper membrane and a 2 mm heater membrane. The bubble size

was difficult to control so again multiple engines were tested at each cavity depth with bubble sizes determined by assembly. Three cavity depths were tested: 75 μm, 150 μm, and 225 μm. The depth was controlled by adding multiple layers of 75 μm thick semiconductor tape to make up the cavity gasket. In this manner, a 225 μm cavity depth was created using 3-layers of semiconductor tape. Upon assembly, the engines were aligned with the vibrometer, and a 200 μs, 3 V heat-pulse was applied to the resistance heater, resulting in an "after-ringing" response of the vibration amplitude of the upper membrane. The bubble size and static deflection were measured within one minute of the free-vibration test. Resonant frequency was determined by fitting a curve to the free-vibration velocity response to the heat pulse.

4.5.2 Cavity Depth Results

Assembling engines at multiple cavity depths proved to be increasingly challenging as the cavity depth increased. The compressibility of the semiconductor tape gasket had a more dramatic effect as more layers were introduced. The compression of the gasket under normal clamping conditions necessary for a proper seal resulted in increased membrane deflection as the cavity volume slightly decreased. Four-millimeter engines assembled with a single layer of 75 mm semiconductor tape had an average static deflection of only 6 μm, with a 95% confidence of 4 μm. Engines assembled with two and three layers of semiconductor tape had an average static deflection of 12 μm and 18 μm with confidence of 7 μm and 10 μm, respectively. The effect of the increased membrane deflection would result in an artificially high resonant frequency measurement as the tension in the membrane increased. Since the static deflections at each cavity depth overlap, the magnitude of the resonant frequency increase due to the increased

membrane tension was not considered upon review of results. The effects of cavity depth on resonant frequency appeared to dominate over any changes in membrane tension.

Resonant frequency was shown to decrease with a decrease in cavity thickness. Figure 4.13 shows the resonant frequency of the three engine configurations tested. These results show that a decrease in cavity thickness behaved like the similar system of structures vibrating in liquids near a solid wall studied by [67] and [58]. In each of these systems, the effective mass of the vibrating structures increased as the depth decreased. In the present study, it is evident that decreasing the thickness results in an increase of the total effective mass of the engine system, and a decrease in resonant frequency.

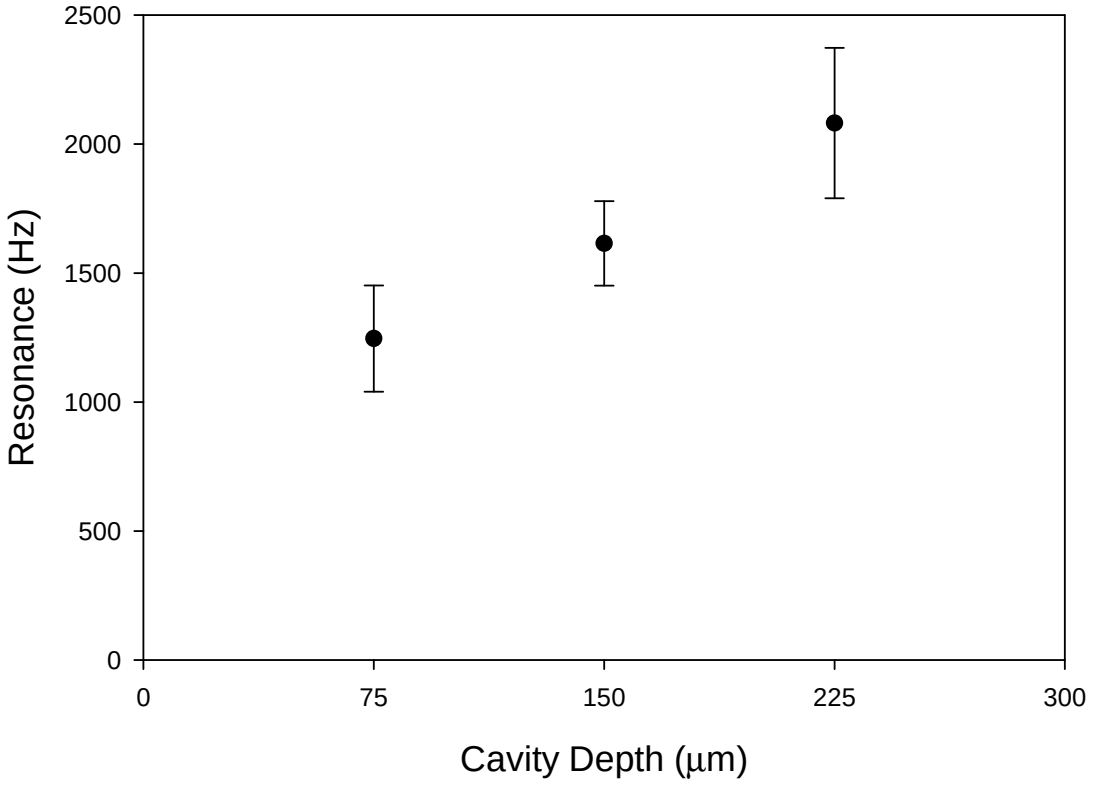

Figure 4.13: Effect of cavity depth on resonant frequency with varying bubble diameters.

CHAPTER 5

ADDED VIRTUAL MASS INCREMENTAL FACTOR MODEL

5.1 AVMI METHOD

Lord Rayleigh showed that the resonant frequency of a vibrating plate in a vacuum could be calculated based on the ratio of the potential energy of the plate to the kinetic energy of the plate in such a way that:

$$\omega_v^2 = \frac{U_P}{T_p} \tag{5.1}$$

where ω is the first resonant mode in rad/sec, U_P is the plate potential energy and T_P is the plates kinetic energy [25]. If the plate is placed in contact with a fluid a decrease in resonant frequency is observed. If it is assumed that the fluid effects do not generate a change in the shape of the plate or its stiffness, the potential energy of the plate in fluid and vacuum remains constant. The ratio of resonant frequency of the plate in fluid to that in a vacuum then becomes:

$$\frac{\omega_f^2}{\omega_v^2} = \frac{T_p}{T_p + T_f} \tag{5.2}$$

where T_f is the added kinetic energy due to the contribution of the fluids inertia [LAMB]. Therefore, the effect of adding fluid to the system is to increase the system inertia by the ratio $(T_p + T_f)/T_p$, or $1 + \beta$, where β, the ratio of the fluid kinetic energy to the plate kinetic energy, is commonly referred to as the added virtual mass incremental (AVMI) factor [49]. The resonant frequency of the plate in fluid is then related to that in a vacuum by:

$$\omega_f = \omega_v \frac{1}{\sqrt{1+\beta}} \tag{5.3}$$

For fully clamped boundary conditions of a circular plate with one surface in contact with fluid, β becomes:

$$\beta = 0.6689 \frac{\rho_f}{\rho_p} \frac{a}{h} \tag{5.4}$$

where ρ_f is the fluid density, ρ_p is the plate density, a is the plate radius, and h is the plate thickness [48]. The coefficient 0.6689 is a constant that accommodates for the mode shape and clamping conditions among other possible outside effects and is often called the non-dimensional added virtual mass incremental (NAVMI) factor denoted by Γ [49]. Kwak also expanded the use of the AVMI method to a circular membrane in contact with fluid under various clamping conditions resulting in a change only to the constant Γ [50]. Later, Kwak studied the effect of fluid depth on a the resonant frequency of a circular plate in contact with fluid, again finding that the AVMI method could hold with only a change in Γ to account for changes in fluid depth proportional to the plate radius [67]. It should stand to reason then, that Γ is independent of the fluid density.

5.2 APPLICATION TO ENGINE

Extrapolating this method to the P3 Engine may provide a method in which the effect of engine parameters on first mode resonant frequency can be explored. If for the engine we take β to be a function of independent separable terms dependent on bubble radius and cavity thickness, respectively, then it holds that:

$$\beta = \alpha(r_B) \cdot \Gamma(t) \tag{5.5}$$

and equation 5.3 becomes:

$$\omega_f = \omega_v \frac{1}{\sqrt{1 + \alpha(r_B) \cdot \Gamma(t)}} \tag{5.6}$$

where r_B and t are the bubble radius and cavity thickness, respectively.

Then,

$$\alpha(r_B) = \frac{\rho_f}{\rho_p} \frac{a}{h} \tag{5.7}$$

where a must be a function of the bubble radius. Since the engine is a fluid system in is appropriate to define a as the hydraulic radius given by the ratio of fluid area in contact with the membrane to the wetted perimeter of the membrane. The relation for alpha to account for how the bubble diameter influences resonant frequency is then given in its final form as:

$$\alpha(r_B) = \frac{\rho_f}{\rho_p} \frac{\left[\frac{L^2 - \pi \cdot r_B^2}{4 \cdot L}\right]}{h} \tag{5.8}$$

where L is the membrane side length. Figure 5.1 shows alpha plotted as a function of bubble diameter for a 4 mm square membrane loaded in an engine.

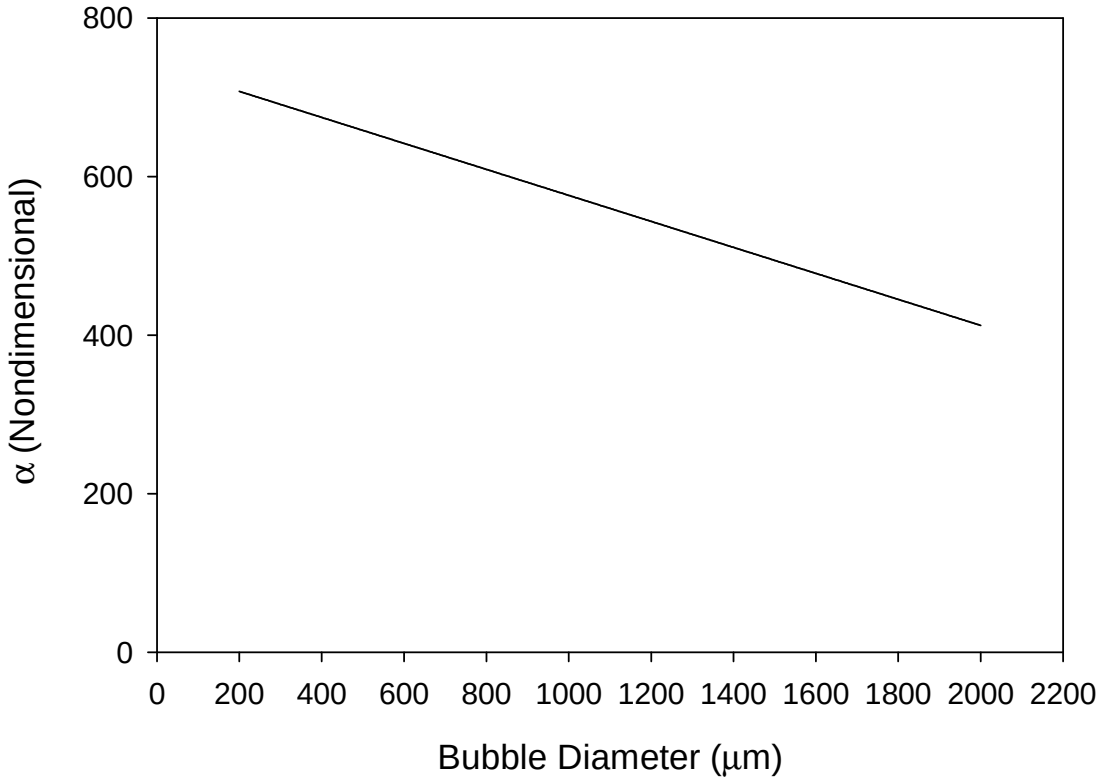

Figure 5.1: Non-dimensional parameter α as a function of bubble diameter for 4 mm Engine.

Next Γ must be expressed as a function of cavity thickness. Γ is inherently a function of clamping conditions, mode shape, cavity thickness, and other secondary effects. Γ can be determined experimentally, by measuring the resonant frequency of a membrane coupled in engines with varying cavity thickness and known bubble diameters. The resonant frequency of the membrane in a vacuum can be calculated using equation 5.9 given by [74] as:

$$f_{11} = \frac{1}{2}\sqrt{\frac{2 \cdot \sigma_0}{\rho \cdot L^2}} \qquad 5.9$$

with: f_{11}: first resonant mode of vibration

σ_0: residual stress

ρ : membrane material density

L: membrane side length

The calculated first mode resonant frequencies based on equation 5.9, with σ_0 = 35 MPa, ρ = 2.3 g/cm^3 and varying membrane side length are shown in Figure 5.2. The only unknown in equation 5.6 is now Γ, which can be determined using the known values.

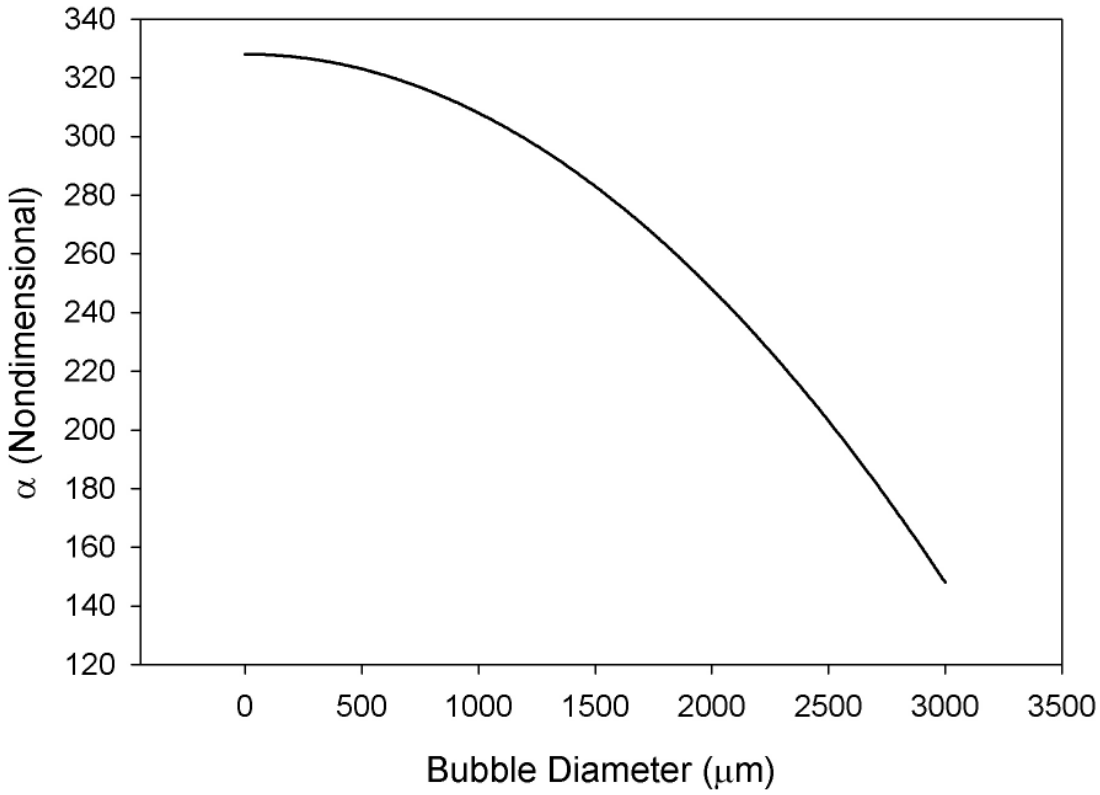

Figure 5.2: Theoretical resonant frequency of silicon membranes with various side lengths in a vacuum.

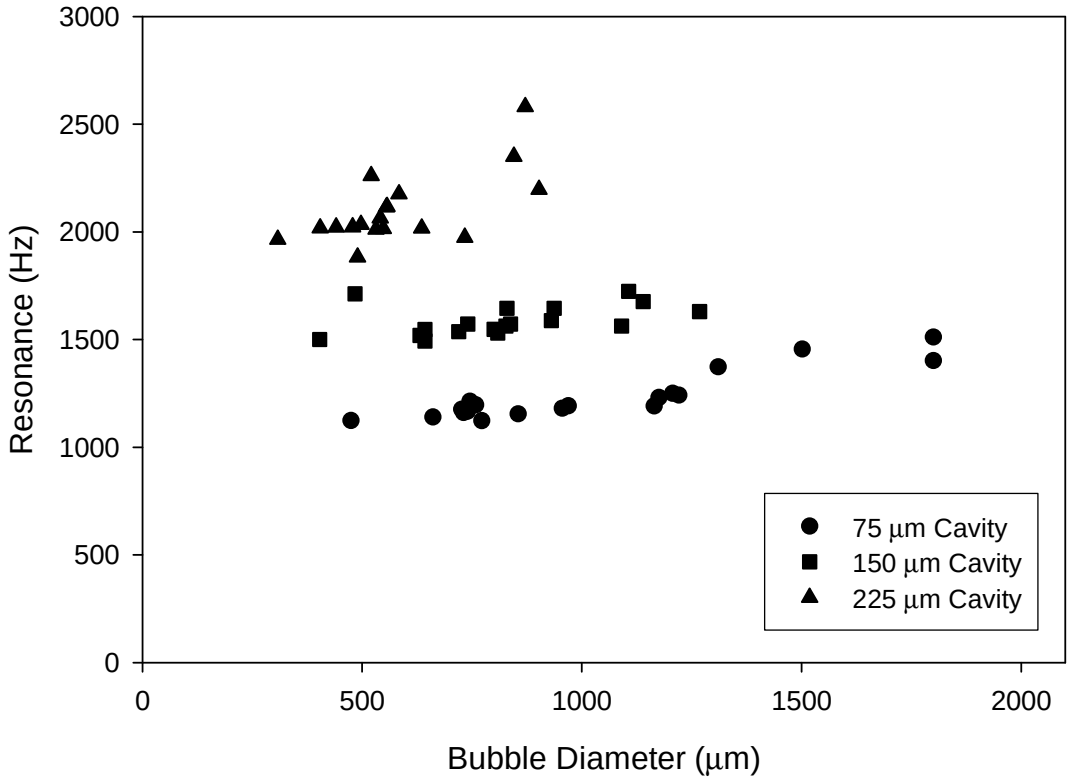

Figure 5.3: Experimental measurement of resonant frequency as a function of bubble diameter for 4 mm engines with cavity depths of 75 μm, 150 μm, and 225 μm.

An experiment was carried out within the parametric study outlined in Chapter 4 in order to determine the effect of cavity thickness on resonant frequency. 4 mm membranes were loaded in engines with cavity thickness of 75, 150, and 225 μm. The bubble diameter for each engine configuration was random, therefore, multiple resonant frequency measurements were made for each configuration and bubble diameters were measured. Figure 5.3 shows the resonant frequency of each configuration versus bubble diameter. Measured resonant frequencies in the engine, bubble diameters, and a calculated resonant frequency in vacuum of 28.9 kHz for the 4 mm membrane, were then used in conjunction with Equation 5.6 to solve for Γ at each engine thickness. Γ was then

averaged at each thickness, and the results are plotted in Figure 5.4 with error bars signifying a 95% confidence interval. An exponential curve fit was then used to extrapolate the effects of other variations in cavity thickness.

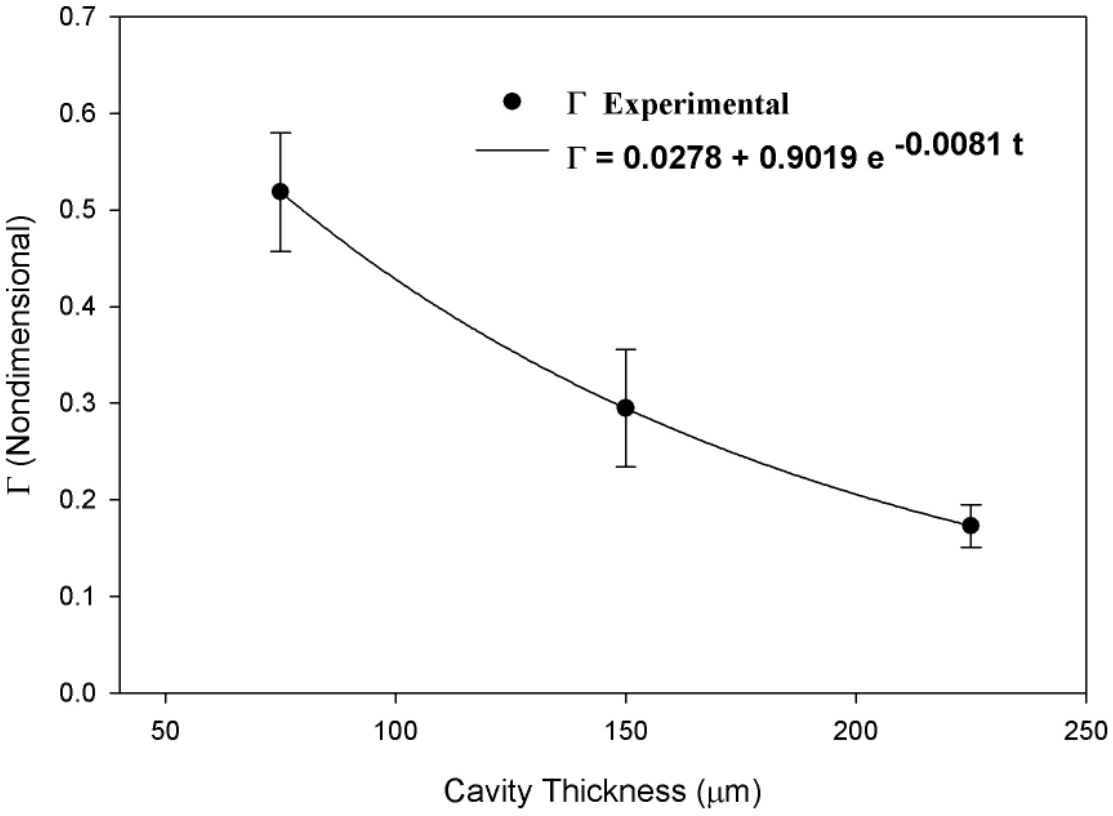

Figure 5.4: AVMI factor Γ as a function of cavity depth with exponential curve fit.

The curves generated for α and Γ were then used to determine the first resonant mode of a 4 mm engine for specific bubble diameters and varying cavity thickness. Trend lines were produced for the three engine configurations tested over a larger range of bubble diameters. As can be seen in Figure 5.5, the curves generated using the AVMI approach fit the data well. Differences are most likely due to engine assembly errors, as the initial deflection of membranes is difficult to control. Also, as shown in the

parametric study of bubble size, there was small increase in resonant frequency as bubble diameter increased due to the area of membrane in contact with fluid. However, there is a much more dramatic effect on resonant frequency due to cavity depth, as shown by the model and experiment.

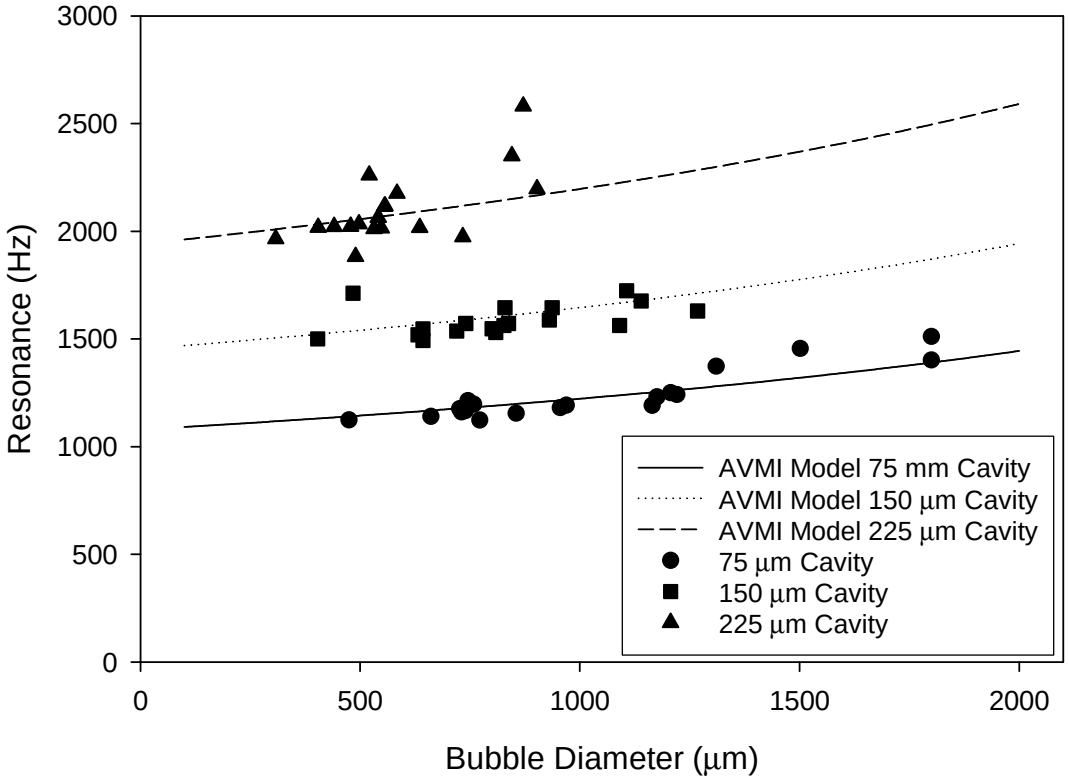

Figure 5.5: AVMI Model fit for resonant frequency approximation with experimental data of 4 mm engines with cavity depths of 75 μm, 150 μm, and 225 μm and varying bubble diameter.

In order to test the ability of the model to extrapolate the resonant frequencies of other engine configurations, it was used to determine the resonant frequency of various engines loaded with various size membranes. Equation 5.6 was used in conjunction with calculated values of membrane resonant frequency in a vacuum, shown in Figure 5.2, α values were calculated for each membrane size over a range of bubble diameters from

Equation 5.8, and Γ values were extrapolated from Figure 5.3, based on a cavity thickness of 150 µm. Two bubble sizes were considered, of 100 µm and 2000 µm, in order to bound the range of bubble diameters typically seen in engines. Figure 5.6, shows the model result compared with experimental data for the mean resonant frequency for a 3 mm, 4 mm, 6 mm, and 8 mm upper membrane loaded in an engine. Inconsistencies in the model are most likely the result of varying initial defections and a limited sample size for larger membranes. The model fits the experimental measurements quite well and can therefore be used as a design tool for creating engines with specific resonant frequency requirements. For convenience, equations used to determine engine resonance are compiled in Table 5.1.

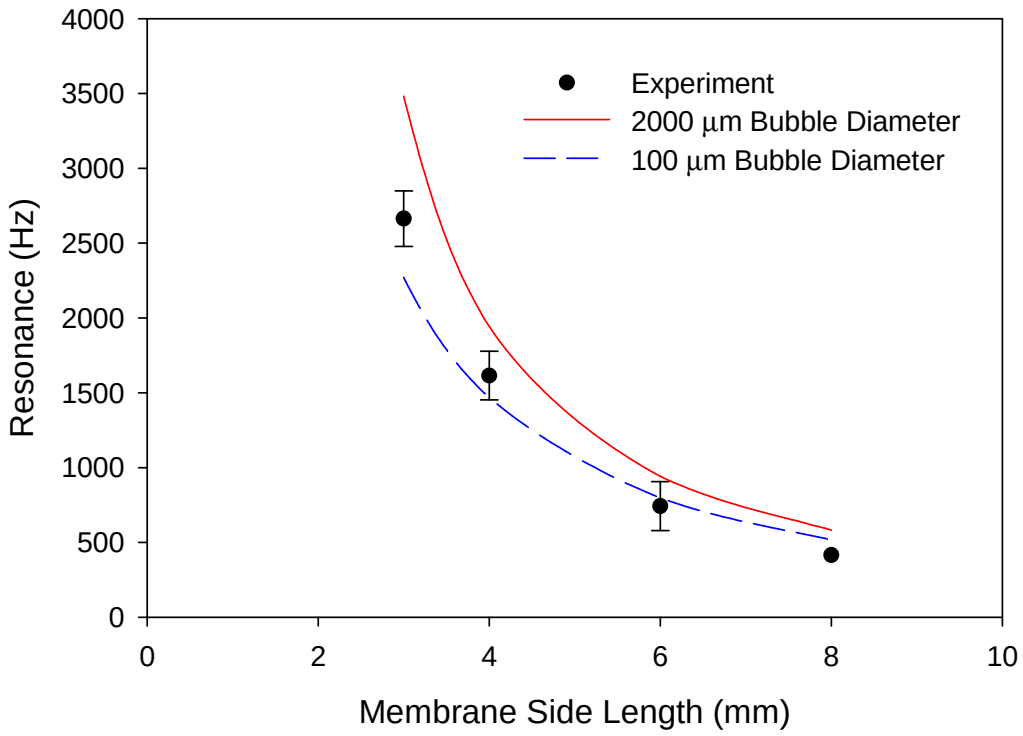

Figure 5.6: AVMI Model fit for resonant frequency approximation of 3 mm, 4 mm, 6 mm and 8 mm engines with 150 µm cavity depth for 500 mm and 2000 mm bubble diameters.

Resonant frequency of engine in Hz	$f_{engine} = f_{vacuum} \frac{1}{\sqrt{1+\alpha \cdot \Gamma}}$	
Resonant frequency of membrane in a vacuum in Hz	$f_{vacuum} = \frac{1}{2}\sqrt{\frac{2 \cdot \sigma_0}{\rho_m \cdot L^2}}$	σ_0 : Membrane residual stress ρ_m : Membrane Density L : Membrane side length
Membrane size and bubble diameter contribution to added mass	$\alpha(r_B) = \frac{\rho_{fluid}}{\rho_m} \frac{\left[\frac{L^2 - \pi \cdot r_B^2}{4 \cdot L}\right]}{h}$	ρ_{fluid} : Fluid Density r_B : Bubble Diameter h : Membrane Thickness
Cavity depth contribution to added mass	$\Gamma = 0.0278 + 0.9019 \cdot e^{-0.0081 \cdot t}$	t : Cavity depth
Typical Values of Constants	σ_0 : 35 MPa (Bare Si Membrane) ρ_m : 2328 kg/m^3 (Si) ρ_{fluid} : 1680 kg/ m^3 (PF-5060) h : 2.2 μm	

Table 5.1: AVMI Model equations and variables.

The AVMI model presented was further extrapolated to provide the necessary engine configurations to yield a desired resonant frequency. Equation 5.6 was used with the left hand side set to 500 Hz. Material properties and bubble size were held constant resulting in only two unknowns – the membrane side length and the NAVMI parameter, Γ. The membrane thickness, residual stress and density were held constant at 2.2mm, 35 MPa, and 2328 kg/m3, respectively. The bubble diameter was held constant at 1000 μm. The membrane side length was used as the independent variable and incrementally varied from 3 mm to 20 mm, allowing for an approximation of Γ. If it is assumed that Γ follows the curve fit in Figure 5.4, the cavity depth for each membrane size can be determined. Figure 5.7 shows the expected membrane side length and cavity depth configurations required to achieve a 500 Hz resonant operating condition. The plot shows that membranes assembled in engines must have side lengths greater than 5 mm for a resonant frequency of 500 Hz. At 6 mm a 15 μm cavity depth would be required which is not practical for engine fabrication. Therefore, a 7.2 mm bare silicon upper membrane is the smallest side length that will operate at 500 Hz, using a single layer of 75 μm thick semiconductor tape to define the engine cavity.

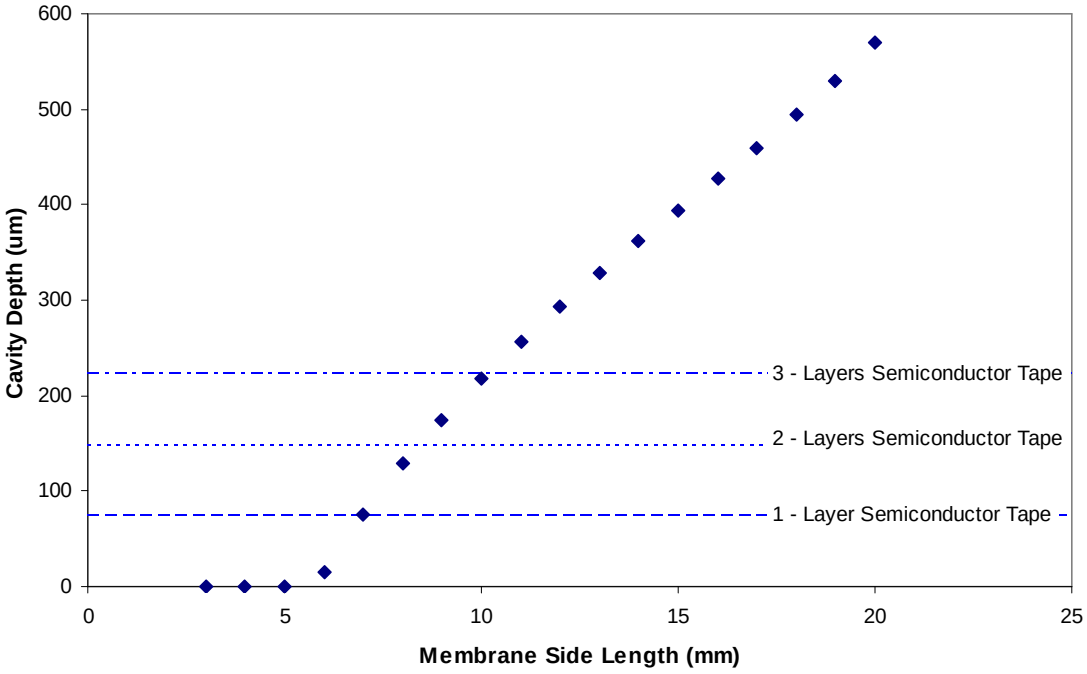

Figure 5.7: Membrane side length and cavity depth required for an engine resonant frequency at 500 Hz.

CHAPTER 6

CONCLUSIONS AND RECOMENDATIONS

6.1 MEASURING RESONANT FREQUENCY

It has been demonstrated that the first resonant mode of vibration for the P3 micro engine can be measured using either a forced-vibration method or a free-vibration method. The forced vibration method involves measuring the vibration amplitude of a generator membrane loaded in an engine as a forcing frequency is applied through the piezoelectric effect of the generator. By measuring the frequency response to a range of frequencies from 2 kHz to 16 kHz, an engine with a 3 mm generator membrane, 150 mm cavity depth, and a 500 μm bubble diameter was shown to have a resonant frequency of 10.1 kHz.

A free-vibration method was also developed to determine the first resonant mode of the engine. This method involved applying an "impact" force to the engine in order measure the "after-ringing" response of the membrane generator. The resonant frequency was then found by fitting a damped sinusoidal function to the "after-ringing" response. The free vibration response of an engine assembled with a 3 mm generator, 150 mm cavity depth, and a 500 μm bubble diameter showed a beating effect most likely due interfering resonant frequency effects from the heater membrane. However, an FFT of the "after-ringing" response showed that the free vibration test could duplicate the forced vibration experiment. In order to eliminate the beating effect an alternate engine configuration was used. This showed that an engine with a silicon membrane of 4 mm side length and 2.2 μm thickness, assembled with a 150 mm cavity depth and an 1170

mm bubble diameter had a resonant frequency of 2037 Hz without noticeable beating. The repeatability of the free vibration test in this configuration was found to be ± 8.6%.

6.2 RESONANT FREQUENCY PARAMETRIC STUDY

Three engine parameters were chosen for their likelihood to influence engine resonant frequency. Namely, the membrane side-length, fluid/vapor ratio as defined by the bubble size, and cavity depth were investigated.

Membrane sizes of 3 mm, 4 mm, 6 mm, and 8 mm were fabricated and assembled in engines. As hypothesized, the resonant frequency dropped as membrane side length increased. Engines assembled with 3 mm silicon membranes, 150 μm cavity depth, and varying bubble size had an average resonant frequency of 2550 Hz. Engines assembled with the same cavity depth and membrane side lengths of 4 mm, 6 mm, and 8 mm had average resonant frequencies of 1615 Hz, 742 Hz, and 416 Hz, respectively. These, results show that tailoring the membrane side length for the specific operating frequency requirements of the engine can effectively control the resonant frequency of the engine to frequencies below 500 Hz.

Bubble diameter was shown to have a small effect on the resonant frequency of the engine. Engines assembled with a 4 mm silicon membrane, 75 μm cavity depth, and varying bubble diameter had resonant frequencies varying from 1110 Hz to 1330 Hz. This showed only ± 8.2% maximum control from a mean of 1208 Hz for bubble diameters ranging from 475 μm to 1500 μm. Because the range of control in bubble diameter is on order with the repeatability error of the free vibration test, at 8.6%, there is

question as to what degree the bubble diameter can be used to perform even small tuning of resonant frequency in the engine.

Three engine cavity depths at 75 μm, 150 μm, and 225 μm for engines assembled with 4 mm silicon membranes and varying bubble diameter. An increase in resonant frequency was seen as the cavity depth was increased. The mean resonant frequencies with 95% confidence for the 75 μm, 150 μm, and 225 μm cavity depths were 1206 ± 206 Hz, 1615 ± 154 Hz, and 2081 ± 291 Hz, respectively. These results show that cavity depth is an effective means of controlling engine resonant frequency.

6.3 AVMI MODEL

The AVMI model was developed in an attempt to quantify the effects of membrane size, bubble diameter, and cavity thickness as virtual mass additions to the relative membrane vibrating in a vacuum. The model operates under the principle that the resonant frequency in a fluid can be related to the resonant frequency in a vacuum by a ratio of each systems kinetic energy. The actual kinetic energy of the fluid-membrane coupling is extremely difficult to solve computationally, therefore the added virtual mass ratio was determined experimentally in two stages. First, the effect of the bubble size was calculated based on the quantity of liquid in contact with the membrane. Then, the effect of the cavity depth was solved from experiments. The cavity depth and bubble diameters effects on resonant frequency were shown to act independently. Results showed that the AVMI parameters dependent on bubble diameter and cavity thickness could be used to predict the resonant frequency of various engine configurations, including changes in membrane size, cavity depth, and bubble diameter. Also, the model

was used to predict the geometry of engine configurations capable of achieving a 500 Hz operating resonant frequency frequency.

6.4 RECOMENDATIONS

One of the most promising methods of controlling resonant frequency was shown to be the membrane side length. However, the greatest challenge in testing membranes over 4 mm was the inability to achieve an adequate seal. Other sealing methods have been attempted including SU-8 resist, various tapes, and silicone rubber with limited success. Also, it has been noted that clamping conditions seem to have a dramatic impact on sealing, because the current carriers in use make it difficult to ensure parallel clamping necessary for a good seal. Therefore there are two paths that may be taken to ensure sealing for large membranes. First, an appropriate gasket material, gasket geometry, or alternative engine fabrication process must be employed to develop a sealed cavity. The second possibility is to improve the carrier clamping method to ensure parallel clamping.

Once a method has been developed to provide adequate sealing, a large membrane (~7 mm) with a reasonably small cavity thickness (~75 μm) should allow for operation of the engine at a resonant frequency near 500 Hz. The engine should then be able to run continuously, albeit at a limited capacity due to insufficient heat rejection. The next logical step is to integrate active cooling of the engine to allow continuous operation and definition of a working thermodynamic cycle. Once a cycle is achieved, the membrane geometry and engine parameters should be optimized in order to provide sufficient inertia for the compression and expansion strokes, as well as overall efficiency.

While the method for active cooling is under development a study should be run to quantify the mechanical losses within the engine. Losses within the engine are suspected to be primarily a result of damping due to the fluid viscosity contributions. A free-vibration test can be used to measure system damping, and an energy balance can be used to determine the system loss during free-vibration. In order to do this effectively, an assembly method must be developed to have better control over engine parameters. Most notably, the initial static deflection of the upper membrane must be consistently controlled to a minimum. Also, a method must be developed to accurately control the fluid/vapor ratio. Once engine losses are quantified, a study should be done to optimize the specific operating resonant frequency resulting in the lowest possible mechanical losses.

The parameters investigated within this research were shown to primarily control the overall mass of the engine system. An additional parameter should also be investigated to determine the effect of system stiffness by controlling the membrane residual stress. This can be accomplished by altering the membrane material, processing, or additional layers to control the composite stiffness.

REFERENCES

1. C. Grosjean, X. Yang, Y. Tai, "A Practical Thermopneumatic Valve", *Proceedings of the 12th IEEE International Conference on Micro Electro Mechanical Systems*, 147-152 (1999).

2. X. Yang, C. Grosjean, Y-C. Tai, C-M. Ho, "A MEMS Thermopneumatic Silicone Membrane Valve", Proceedings of the IEEE Micro Electro Mechanical Systems (MEMS), 114-118 (1997).

3. C. Grosjean, Y.C. Tai, "A Thermopneumatic Peristaltic Micropump", *Proceedings of the International Conference on Solid-State Sensors and Actuators*, 1776-1779 (1999).

4. O.C. Jeong, S.S. Yang, "Fabrication and Test of a Thermopneumatic Micropump with a Corrugated p+ Diaphragm", *Sensors and Actuators* **83**, 249-255 (2000).

5. F.C.M. Van De Pol, H.T.G Van Lintel, M. Elwenspoek, J.H.J Fluitman, "A Thermopneumatic Micropump Based on Micro-engineering Techniques", *Sensors and Actuators A* **21-23**, 198-202 (1990).

6. M. Carmona, S. Marco, J. Samitier, J.R. Morante, "Dynamic Simulations of Micropumps", *Journal of Micromechanics and Microengineering* **6**, 128-130 (1996).

7. M. Carmona, S. Marco, J. Samitier, "Modeling the Thermal Actuation in a Thermo-Pneumatic Micropump", *Journal of Electronic Packaging* **125**, 527-530 (2003).

8. C.D. Richards, D.F. Bahr, R.F. Richards, "A Micro Heat Engine for MEMS Power", *American Society of Mechanical Engineers, Fluids Engineering Division (Publication) FED* **258**, 501-509 (2002).

9. J. McEntee, L. Bowman, "Oscillating Diaphragms", *Proceedings of the International Conference on Modeling and Simulation of Microsystems* **2**, 597-600 (1999).

10. S. Kang, S. Tsai, H. Chen, "Fabrication and Test of Radial Grooved Micro Heat Pipes", *Applied Thermal Engineering* **22**, 1559-1568 (2002).

11. P.D. Dunn, D.A. Reay, Heat Pipes, Pergamon, Oxford, 4-5 (1994).

12. B. Marland, D. Bugby, C. Stouffer, "Development and Testing of Advanced Cryogenic Thermal Switch Concepts", Proceedings of the Space Technology and Applications International Forum, 837-846 (2000).

13. A.O. Christensen, J.P. Jacob, C.D. Richards, D.F. Bahr, R.G. Richards, "Fabrication and Characterization of a Liquid-Metal Micro-Droplet Thermal Switch", *Proceedings of Transducers'03,* Paper No. AM069, Boston, (2003).

14. C.D Richards, D.F. Bahr, C.-G. Xu, R.F. Richards, "MEMS Power: The P^3 System", *Proceedings of the Intersociety Energy Conversion Engineering Conference* **2**, 803-814 (2001).

15. S. Whalen, M. Thompson, D.F. Bahr, C.D. Richards, R.F. Richards, "Design, Fabrication, and Testing of the P^3 Micro Heat Engine", *Sensors and Actuators A* **104**, 290-298 (2003).

16. L.S. Pan, T.Y. Ng, X.H. Wu, H.P. Lee, "Analysis of Valveless Micropumps with Inertial Effects", *Journal of Micromechanics and Microengineering* **13**, 390-399 (2003).

17. A. Ullmann, I. Fono, "The Piezoelectric Valve-Less Pump – Improved Dynamic Model", *Journal of Microelectromechanical Systems* **11**, 655-664 (2002).

18. J-H. Park, K. Yoshida, S. Yokota, "Resonantly Driven Piezoelectric Micropump Fabrication of a Micropump Having High Power Density", *Mechatronics* **9**, 687-702 (1999).

19. A. Caronti, G. Caliano, A. Iula, M. Pappalardo, "An Accurate Model for Capacitive Micromachined Ultrasonic Transducers", *IEEE Transactions on Ultrasonics, Ferroelectrics, and Frequency Control* **49**, 159-168 (2002).

20. J, Hietanen, Capacitive Ultrasonic Transducers: Their Parameters and Testing, Acta Scandinavica, Applied Physics Series No. 209, Helsinki (1999).

21. S.T. Hansen, A. Turo, F.L. Degertekin, B.T. Khuri-Yakub, "Characterization of Capacitive Micromachined Ultrasonic Transducers in Air Using Optical Measurements", *Proceedings of the IEEE Ultrasonics Symposium*, 947-950 (2000).

22. E. Defay, C. Millon, C. Malhaire, D. Barbier, "PZT Thin Films Integration for the Realisation of a High Sensitivity Pressure Microsensor Based on a Vibrating Membrane", *Sensors and Actuators A* **99**, 64-67 (2002).

23. G. Caliano, N. Lamberti, A. Iula, M. Pappalardo, "A Piezoelectric Bimorph Static Pressure Sensor", *Sensors and Actuators A* **46-47**, 176-178 (1995).

24. R.L. Bardell, N.R. Sharma, F.K. Forster, M.A. Afromowitz, R.J. Penney, "Designing High-Performance Micro-Pumps Based on No-Moving-Parts Valves", *ASME, Dynamic Systems and Control Division DSC*, v 62, *Microelectromechanical Systems (MEMS)*, 47-53 (1997).

25. J.W.S. Rayleigh, The Theory of Sound, Volume 1, Dover Publications, New York (1945).

26. S. Timoshenko, S. Woinowsky-Krieger, Theory of Plates and Shells, McGraw-Hill, New York (1959).

27. R. Paneva, D. Gotchev, "Non-Linear Vibration Behavior of Thin Multilayer Diaphragms", *Sensors and Actuators A* **72**, 79-87 (1999).

28. K. El Bikri, R. Benamar, M. Bennouna, "Geometrically Non-Linear Free Vibrations of Clamped Simply Supported Rectangular Plates. Part I: The Effects of Large Vibration Amplitudes on the Fundamental Mode Shape", *Computers and Structures* **81**, 2029-2043 (2003).

29. H. Koivurova, A. Pramila, "Nonlinear Vibration of Axially Moving Membrane by Finite Element Method", *Computational Mechanics* **20**, 537-581 (1997).

30. W.A. Moussa, U.F. Gonzalez, "Simulation of MEMS Piezoelectric Micropump for Biomedical Applications", *Proceedings of the International Mechanical Engineering Congress and Exposition*, 187-192 (2002).

31. A. Olsson, G. Stemme, E. Stemme, "The First Valve-Less Diffuser Gas Pump", *Proceedings of the IEEE Micro Electro Mechanical Systems (MEMS)*, 108-113 (1997).

32. P. Rangsten, L. Smith, L. Rosengren, B. Hok, "Electrostatically Excited Diaphragm Driven as a Loudspeaker", *Sensors and Actuators A* **52**, 211-215 (1996).

33. G.T.A. Kovacs, Micromachined Transducer Sourcebook, McGraw Hill, Boston, 289-295 (1998).

34. M. Arik, S.M. Zurn, K.S. Yigit, A. Bar-Cohen, "Design, Fabrication and Experimental-Numerical Study of PZT Sensors", *Proceedings of the International Conference on Modeling and Simulation of Microsystems*, 574-578 (2000).

35. R.D. Blevins, Formulas for Natural Frequency and Mode Shape, Van Nostrand Reinhold Co., New York, 224-232, 386-424 (1979).

36. B. de Heij, B. van der Schoot, N.F. de Rooij, H. Bo, J. Hess, "Modelling and Optimisation of a Vaporiser for Inhalation Drug Therapy", *Proceedings of the International Conference on Modeling and Simulation of Microsystems*, 542-545 (1999).

37. S.C. Ko, Y.C. Kim, S.S. Lee, S.H. Choi, S.R. Kim, "Micromachined Piezoelectric Membrane Acoustic Device", *Sensors and Actuators A* **103**, 130-134 (2003).

38. P. Muralt, A. Kholkin, M. Kohli, T. Maeder, "Piezoelectric Actuation of PZT Thin-Film Diaphragms at Static and Resonant Conditions", *Sensors and Actuators A* **53**, 398-404 (1996).

39. J. Thomas, R. Kuhnhold, R. Schnupp, G. Temmel, H. Ryssel, "Simulation of the Production of Functional Layers for Vibration Sensors for Tool State Monitoring and Finite Element Analysis of Mechanical Characteristics", *Proceedings of the International Conference on Modeling and Simulation of Microsystems* **2**, 593-596 (1999).

40. A. Degen, N. Abedinov, T. Gotszalk, E. Sossna, M. Kratzenberg, I.W. Rangelow, "Stress Analysis in Si Membranes for Open Stencil Masks and Mini-Reticles Using Double Bulging and Resonant frequency Methods", *Microelectronic Engineering* **57-58**, 425-432 (2001).

41. M.S. Kennedy, D.F. Bahr, C.D. Richards, R.F. Richards, "Residual Stress Control to Optimize PZT MEMS Performance", *Proceedings of the Materials Research Society Symposium* **741**, 163-168 (2002).

42. J.S. Kim, K. Choi, I. Yu, "A New Method of Determining the Equivalent Circuit Parameters of Piezoelectric Resonators and Analysis of the Piezoelectric Loading Effect", *IEEE Transactions on Ultrasonics, Ferroelectrics, and Frequency Control* **40**, 424-426 (1993).

43. L. Pizarro, D. Certon, M. Lethiecq, O. Boumatar, B. Hosten, "Experimental Investigation of Electrostatic Ultrasonic Transducers with Grooved Backplates", *Proceedings of the IEEE Ultrasonics Symposium* **2**, 1003-1006 (1997).

44. J. Billingham, "Modelling the Response of a Vibrating-Element Density Meter in a Two-Phase Mixture", *Journal of Fluid Mechanics* **340**, 343-360 (1997).

45. D. Crescini, D. Marioli, A. Taroni, "Piezoelectric Thick-Film Fluid Density Sensor Based on Resonant frequency Vibration", *Proceedings of the IEEE Instrumentation and Measurement Technology Conference*, 1368-1371 (1998).

46. C.T. Crowe, D.F. Elger, J.A. Roberson, Engineering Fluid Mechanics, 7th Ed. John Wiley and Sons. (2001).

47. S.Inaba, K. Akaishi, T. Mori, K. Hane, "Analysis of the Resonant frequency Characteristics of a Cantilever Vibrated Photothermally in a Liquid", *Journal of Applied Physics* **73**, 2654-2658 (1993).

48. H. Lamb, "On the Vibrations of an Elastic Plate in Contact with Water", *Proceedings of The Royal Society* **98**, 205-216 (1920).

49. M.K. Kwak, K.C. Kim, "Axisymmetric Vibration of Circular Plates in Contact with Fluid", *Journal of Sound and Vibration* **146**, 381-389 (1991).

50. M.K. Kwak, "Vibration of Circular Membranes in Contact with Water", *Journal of Sound and Vibration* **178**, 688-690 (1994).

51. M.S. Weinberg, C.E. Dube, A. Petrovich, A.M. Zapata, "Fluid Damping in Resonant Flexural Plate Wave Device", *Journal of Microelectromechanical Systems* **12**, 567-596 (2003).

52. M. Amabili, "Effect of Finite Fluid Depth on the Hydroelastic Vibrations of Circular and Annular Plates", *Journal of Sound and Vibration* **193**, 909-925 (1996).

53. A. Prak, F.R. Blom, M. Elwenspoek, T.S.J. Lammerink, "Q-Factor and Frequency Shift of Resonating Silicon Diaphragms in Air", *Sensors and Actuators A* **25-27**, 691-698 (1991).

54. Y.K. Cheung, D. Zhou, "Coupled Vibratory Characteristics of a Rectangular Container Bottom Plate", *Journal of Fluids and Structures* **14**, 339-357 (2000).

55. Y. Fu, W.G. Price, "Interactions Between a Partially or Totally Immersed Vibrating Cantilever Plate and the Surrounding Fluid", *Journal of Sound and Vibration* **118**, 495-513 (1987).

56. G. Muthuveerappan, N. Ganesan, M.A. Veluswami, "Note on Vibration of a Cantilever Plate Immersed in Water", *Journal of Sound and Vibration* **63**, 385-391 (1979).

57. M.S. Marcus, "Finite-Element Method Applied to the Vibration of Submerged Plates", *Journal of Ship Research* **22**, 94-99 (1978).

58. T. Naik, E.K. Longmire, S.C. Mantell, "Dynamic Response of a Cantilever in Liquid Near a Solid Wall", *Sensors and Actuators A* **102**, 240-254 (2003).

59. F. Montero de Espinosa, J.A. Gallego-Juarez, "On the Resonant frequency Frequencies of Water-Loaded Circular Plates", *Journal of Sound and Vibration* **94**, 217-222 (1984).

60. L. Jezequel, "Hydrodynamic Added-Mass Identification from Resonance Tests", *AIAA Journal* **21**, 608-613 (1983).

61. A. Olsson, G. Stemme, E. Stemme, "A Valve-Less Planar Fluid Pump with Two Pump Chambers", *Sensors and Actuators A* **46-47**, 549-556 (1995).

62. L.S. Pan, T.Y. Ng, G.R. Liu, K.Y. Lam, T.Y. Jiang, "Analytical Solutions for the Dynamic Analysis of a Valveless Micropump – a Fluid-Membrane Coupling Study", *Sensors and Actuators A* **93**, 173-181 (2001).

63. S. Inaba, K. Hane, "Dependence of Resonant frequency Frequency of a Membrane Vibrated Photothermally on Pressure and Geometry in a Low-Vacuum Region", *Japanese Journal of Applied Physics* **32**, 1001-1004 (1993).

64. J. Mertens, E. Finot, T. Thundat, A. Fabre, M-H. Nadal, V. Eyraud, E. Bourillot, "Effects of Temperature and Pressure on Microcantilever Resonant frequency Response", *Ultramicroscopy* **97**, 119-126 (2003).

65. W.P. Lai, W. Fang, "A Novel Antistiction Method Using Harmonic Excitation on the Microstructure", *Journal of Vacuum Science Technology A* **19**, 1224-1228 (2001).

66. T. Abe, W.C. Messner, M.L. Reed, "Effects of Elevated Temperature Treatments on Microstructure Release Procedures", *Journal of Microelectromechanical Systems* **4**, 66-75 (1995).

67. M.K. Kwak, S.-B. Han, "Effect of Fluid Depth on the Hydroelastic Vibration of Free-Edge Circular Plate", *Journal of Sound and Vibration* **230**, 171-185 (2000).

68. A. Olson, MS Thesis, Washington State University (2003).

69. J. Kanyer, MS Thesis, Washington State University (2003).

70. K. Bruce, R. Richards, D. Bahr, C. Richards, "Characterization of a Piezoelectric Membrane for MEMS Power", *Proceedings of ASME International Mechanical Engineering Congress and Exposition* **3**, 21-28 (2001).

71. Polytec GmbH, *User Manual: Vibrometer Controller OFV-5000*, Waldronn, Germany. (2003).

72. F.P. Beer, E.R. Johnston, Vector Mechanics for Engineers: Dynamics, 6^{th} Ed. McGraw Hill, (1997).

73. J.H. Cho, M.J. Anderson, D.F. Richards, D.F. Bahr, C.D. Richards, "Analysis of Micromachined PZT Membranes for MEMS Power," *Proceedings of Nanotech'04* **1**, 382-385 (2004).

74. R. Szilard, Theory and Analysis of Plates: Classical and Numerical Methods, Prentice Hall, 421 (1974).

75. Internet Source: “Experiment 31: Using Excel to Compute FFT”, http://www.mme.wsu.edu/~me305/exp31.htm

76. S.A. Whalen, M.R. Thompson, C.D. Richards, D.F. Bahr, R.F. Richards, “Low Frequency Operation of the P3 Micro Heat Engine”, *Proceedings of International Mechanical Engineering Congress and Exposition*, 469-476 (2002).

77. A.J. Wheeler, A.R. Ganji, Introduction to Engineering Experimentation, Prentice Hall, Upper Saddle River, New Jersey, 138-163 (1996).